Chapter 5

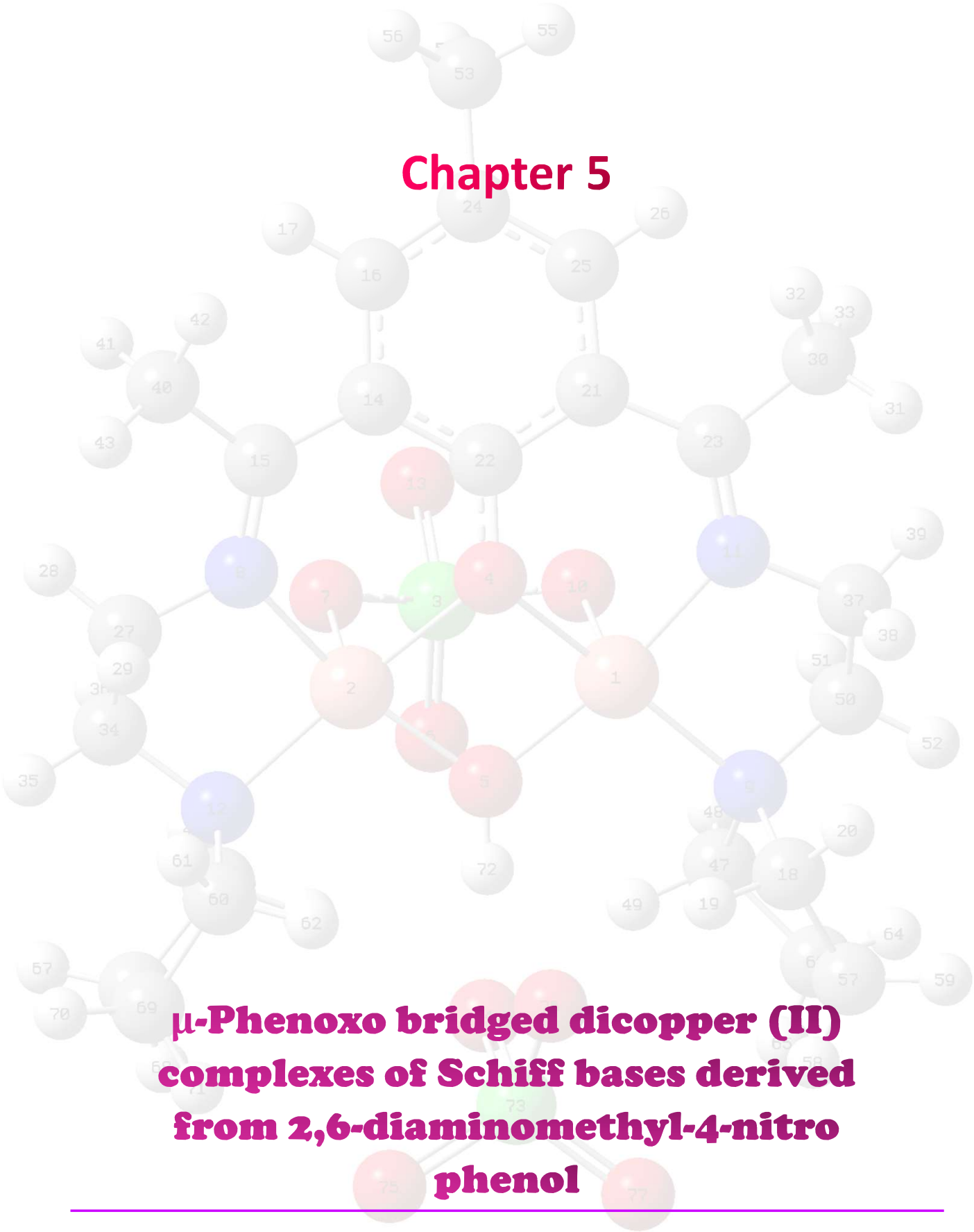

μ-Phenoxo bridged dicopper (II) complexes of Schiff bases derived from 2,6-diaminomethyl-4-nitro phenol

Chapter 5: μ-phenoxo bridged dicopper(II) complexes of compartmental Schiff bases derived from 2,6-bis(aminomethyl)-4-nitrophenol

5.1 Introduction 270

5.2 Experimental Section 273

5.2.1 Materials and Methods 273

5.2.2 Synthesis of the Schiff base ligand (L^{13}-L^{14}) 273

5.2.3 Synthesis of the binuclear copper complexes (C13-C16) 275

5.2.4 SOD mimic activity 276

5.2.5 Ascorbic Acid Oxidase (AAO) activity 276

5.2.6 Catecholase activity 277

5.2.5 Physical Measurements 279

5.2.5.1 Infrared studies 279

5.2.5.2 NMR studies 279

5.2.5.3 Mass studies 279

5.2.5.4 Electronic studies 279

5.2.5.5 Photoluminescence studies 279

5.2.5.6 Elemental Analysis 279

5.2.5.7 ESR studies 279

5.2.5.8 Molecular modelling 279

5.3 Results and Discussion 280

5.3.1 Characterization of ligands 280

5.3.1.1 IR spectroscopy 280

5.3.1.2 NMR Spectroscopy 280

5.3.1.3 Electronic spectra 281

5.3.1.4 Photoluminescence spectra 281

5.3.1.5. Mass Spectra 282

5.3.2 Characterization of complexes 282

5.3.2.1 Elemental analysis 282

5.3.2.2 IR spectra 282

5.3.2.3 Mass spectra 283

5.3.2.4 Electronic spectroscopy 284

5.3.2.5 Photoluminescence spectra 285

5.3.2.6 ESR spectra 286

5.3.2.7 Molecular Modelling 287

5.3.3 SOD mimic activity of the complexes 293

5.3.4 Ascorbic Acid Oxidase (AAO) activity 296

5.3.5 Catecholase activity 301

5.4 CONCLUSION 308

Supporting Information 309

REFERENCES 329

5.1 Introduction

The most challenging problem of modelling the binuclear active sites in copper proteins is to duplicate the intermetallic distance and attain a lower activation energy path for the reactions by achieving a coordination geometry which can lead to a reversible redox. Most model dinuclear compounds fail to reproduce this essential feature of metalloproteins. To mimic these active sites, use of classical Robson unit, 2,6-dimino-4-methylphenol, or incorporation of two tripodal groups onto 2,6-dimethylphenol have been reported. In both cases, the intermetallic distance cannot be longer than 3.3 Å. This separation can also be achieved by a system involving a 3-hydroxypropyl group giving high flexibility to the overall ligand system. This system was incorporated by us in chapter 4 for the synthesis of copper(II) complexes. Another interesting feature of the ligand system was thought to be an effort to bring in flexibility around the bridging phenolate by way of removing unsaturation in the adjacent part of the ligand and balancing electronic characteristics by using an electron withdrawing group in place of electron releasing methyl in the Robson unit.

A thought of the above considerations lead us to a path to investigate the chemistry of dicopper(II) complexes derived from Schiff bases of 2,6-bis(aminomethyl)-4-nitrophenol.[1,2] the above mentioned ligand system has a free rotation around the methylene group which allows for geometrical distortions and accommodations of long Cu---Cu separation is expected.

Very few similar complexes have been reported in the literature. Bailey *et al*[3] obtained adventitious self-assembly of hexanuclear copper(II) aggregate $[\{Cu_3L(OH)(dmf)\}_2(\mu\text{-}Cl)\text{-}(\mu\text{-}L)]\cdot 2dmf$ (dmf= dimethylformamide) during recrystallization of dinuclear copper(II) hydroxo complex derived from 4-nitro-2,6-bis[(salicylideneamino)methyl)]phenol (H_3L) (**Scheme 5.1.1**). Magnetic property of the system was reported. But its complexity leaves uncertainty in predicting its magnetic properties due to inherent weakness of the technique to deal with high nuclearity clusters.

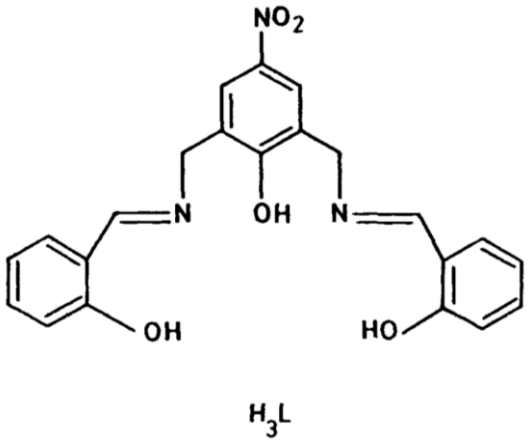

Scheme 5.1.1 *Structure of ligand H_3L(Ref[1])*

Kumar *et al*[4] synthesized homodinuclear Lanthanide(III) complexes $[Ln_2(H_4L^4)(NO_3)(CH_3CN)(](NO_3)_2 \cdot nH_2O$ (Ln= La, Eu, Gd, Tb or Dy; n= 3,4 or 5) of the 24 membered tetraimine phenolic macrocycle of H_4L^4 prepared by condenstation of 2,6-diformyl-4-methylphenol and 2,6-bis(aminomethyl)-4-nitrophenol in presence of hydrated lanthanide(III) nirates. They also synthesized lanthanide(III) complexes $[Ln_2(H_2L^5)(NO_3)_x\ (H_2O)_y](NO_3)_z \cdot nH_2O$ (Ln= La, Pr, Nd, Sm, Eu, Gd or Dy; x=3 or 4; y=0 or 1; z=2 or 3;n=1-4) and $[Ln_2(L^5)(NO_3)_x](NO_3)_y \cdot nH_2O$ (Ln=Tb, Ho or Er; x=2 or 3; y=1 or 2; n= 1 or 2) of a 34 membered octaaza macrocycle obtained by the condensation of 2,6-diformyl-4-methylphenol with 1,2-bis(3-aminopropylamino)- ethane in presence of hydrated Lanthanide(III) nitrates (**Scheme 5.1.2**).[4]

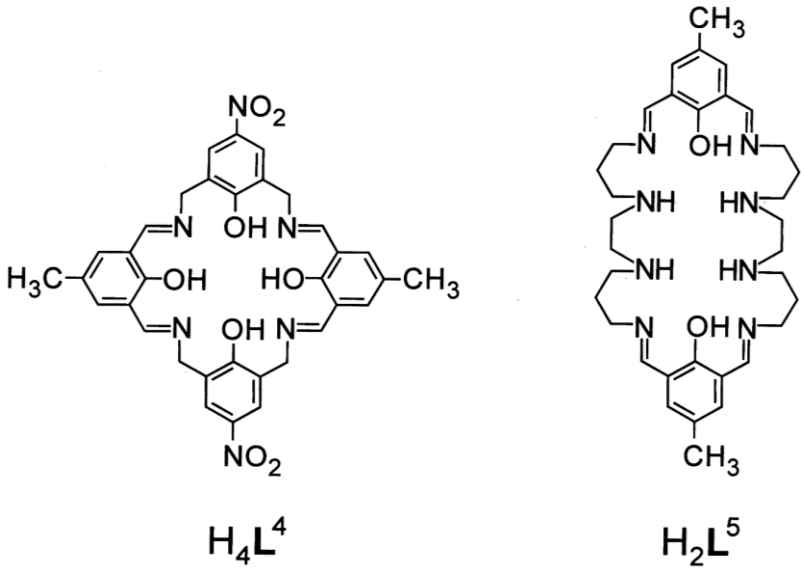

Scheme 5.1.2 *Structure of ligand H_4L^4 and H_2L^5(Ref[4])*

In the present work, binucleating Schiff bases were formed by condensation of 2,6-bis(aminomethyl)-4-nitrophenol with substituted o-hydroxy acetonaphthones, 2-formyl pyrrole and 8-formyl-7-hydroxy-4-methyl coumarin. These binucleating moieties provide a bridging phenoxide group along with phenoxo oxygen and imine nitrogen atoms for coordination with the metal ions. Herein, we report the synthesis and characterization of four binucleating copper(II)-μ-phenoxo-μ-acetate bridged complexes (*viz.* $[Cu_2(L_{13})(OAc)]$ (**C13**), $[Cu_2(L_{14})(OAc)]$ (**C14**), $[Cu_2(L_{13})_2](OAc)_2$ (**C15**) and $[Cu_2(L_{16})(OAc)]$ (**C16**)) of binucleating Schiff bases (**L^{13}-L^{16}**) (**Scheme 5.1.3**) which acts as a structural and functional models for the active site of catechol oxidase, ascorbate oxidase and SOD mimics.

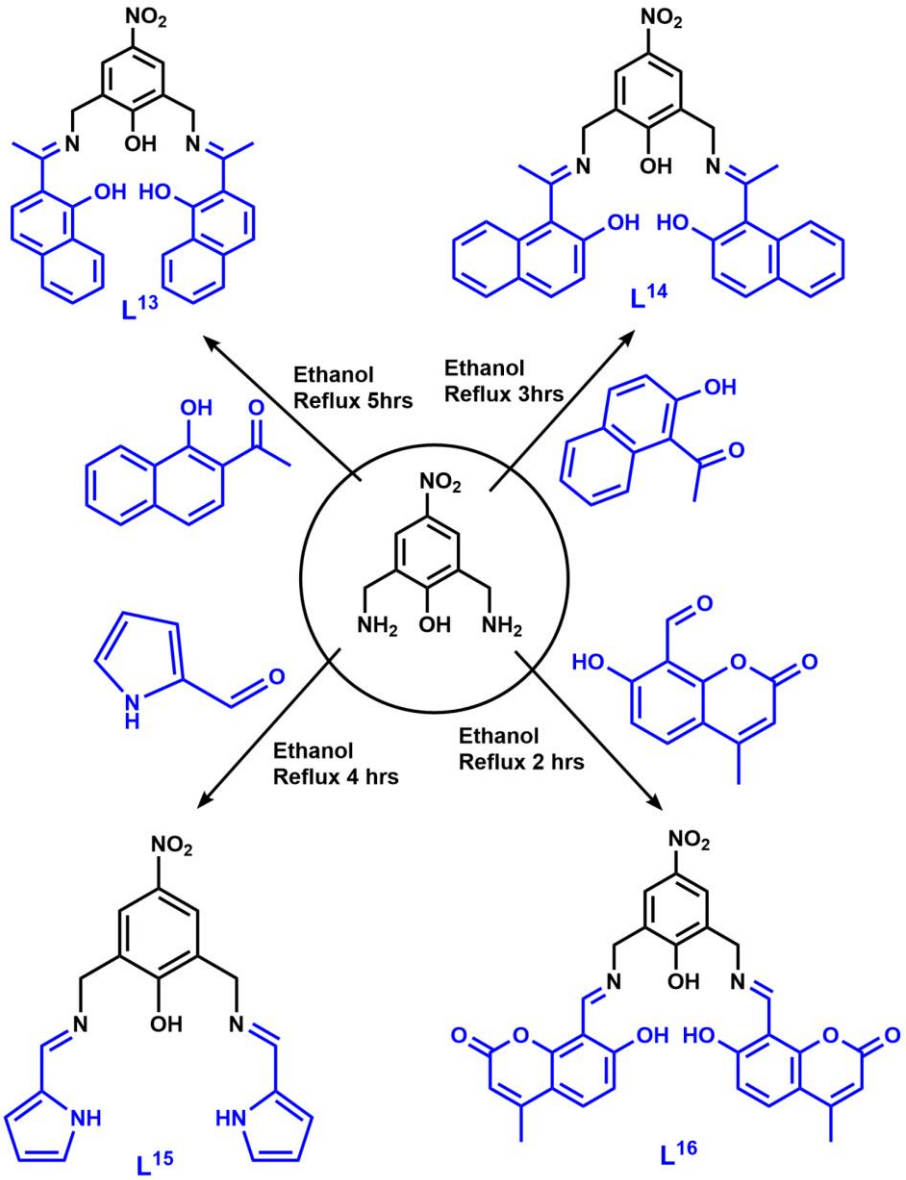

Scheme 5.1.3 *Schematic representation of synthesized ligands* ***L^{13}-L^{16}***

The catecholase and ascorbic acid oxidase activity of these complexes have been studied by using appropriate substrates and compared with known catecholase mimics. Molecular modelling at density functional theory (DFT) level has been utilized to get an insight into the electronic and molecular structures of these synthesized complexes. The SOD mimetic activity of the complexes was also explored. The results of the above-mentioned investigations have been discussed in this chapter.

5.2 Experimental Section

5.2.1 Materials and Methods

Copper acetate monohydrate, hexamine and hydrazine hydrate were procured from Merck. 1-hydroxy-2-acetonaphthone, 2-hydroxy-1-acetonaphthone, 2-formyl pyrrole, 3,5-DTBC, 4-methyl catechol, dopamine, pyrocatechol, 2,3-dihydroxy naphthalene have been purchased from Sigma Aldrich. Potassium iodide and ammonium molybdate were purchased from Loba Chem. Phthalimide, p-nitrophenol, diethyl ether, β-NADH, phenazine methosulphate (PMS), nitroblue tetrazolium (NBT), acetic acid, sodium dihydrogen phosphate monohydrate and dibasic sodium phosphate (anhydrous), 7-hydroxy-4-methylcoumarin were procured from SRL chemicals. 8-formyl-7-hydroxy-4-methylcoumarin[5] and 2,6-bis(aminomethyl)-4-nitrophenol[3] were prepared using literature method. Methanol and dimethyl sulfoxide have been procured from Spectrochem. All chemicals used were of AR grade and were used as received. For spectroscopic studies, spectroscopic grade solvent was used. The solvents have been distilled prior to use and dried according to standard procedure wherever necessary.

5.2.2 Synthesis of the Schiff base ligand (L^{13}-L^{14})

Ligand **L^{13}**: 2,6-bis(aminomethyl)-4-nitrophenol dihydrochloride (0.135g, 0.5mmol) was suspended in methanol (5ml) and treated with a methanolic solution (2ml) of potassium hydroxide (0.056g, 1mmol). The resulting solution was allowed to reflux for 15 mins. After 15 mins, the resulting suspension (precipitated potassium chloride) was filtered and the filtrate was added dropwise to the hot methanolic solution (5ml) of 1-hydroxy-2-acetonaphthone (0.186g, 1mmol) in a RB flask. The mixture was allowed to reflux for 5 hours and the reaction was monitored with the help of TLC. At the end of 5 hours, a single spot for the product appeared on TLC.

Within few hours, yellow microcrystalline solid precipitated out from the solution. The reaction mixture was concentrated to about 10 ml and cooled to obtain yellow microcrystalline solid. The product was filtered and washed with cold ethanol to remove the traces of any soluble impurities and unreacted starting compounds. No further purification method was employed as the product gave a single spot in TLC. Yield = 0.0637g (24.02%). Solubility: DMSO, DMF. M.P.: 280°C (decomp.)

Ligand **L^{14}**: The procedure for the synthesis was analogous to the synthesis of ligand **L^{13}** using methanolic solution (5ml) of 2-hydroxy-1-acetonaphthone (0.186g, 1mmol). The mixture was allowed to reflux for 3 hours by monitoring with the help of TLC. At the end of 3 hours, a single spot for the product appeared on TLC. The reaction mixture was concentrated to about 10 ml and cooled to obtain yellow-orange microcrystalline solid. The product was filtered and washed with cold ethanol to remove the traces of any soluble impurities and unreacted starting materials if any. No further purification method was employed as single spot was obtained on TLC plate. Yield = 0.0449g (16.85%). Solubility: DMSO. M.P.: 220-222°C

Ligand **L^{15}**: The procedure for the synthesis was analogous to the synthesis of ligand **L^{13}** using methanolic solution (5ml) of 2-formylpyrrole (0.095g, 1mmol). The mixture was allowed to reflux for 4 hours by monitoring with the help of TLC. At the end of 4 hours, a single spot for the product appeared on TLC. The reaction mixture was concentrated to about 10 ml and cooled to obtain brownish orange microcrystalline solid. The product was filtered and washed with cold ethanol to remove the traces of any soluble impurities and unreacted starting compounds. No further purification was carried out as a single spot was obtained on TLC plate. Yield = 0.095g (54.13%). Solubility: DMSO. M.P.: 262°C (decomp.)

Ligand **L^{16}:** The procedure for the synthesis was analogous to the synthesis of ligand **L^{13}** but with methanolic solution (10ml) of 2,6-bis(aminomethyl)-4-nitrophenol (0.270g, 1mmol) and KOH (0.112g, 2mmol) and 8-formyl-7-hydroxy-4-methyl coumarin (0.408g, 2mmol). The mixture was allowed to reflux for 2 hours during which time the progress of the reaction was monitored with the help of TLC. At the end of 2 hours, a single spot for the product appeared on TLC. The reaction mixture was concentrated to about 10 ml and cooled to obtain yellow microcrystalline solid.

The product was filtered and washed with cold ethanol to remove the traces of any soluble impurities and unreacted reactants. No further purification was required as a single spot was obtained on TLC plate. Yield = 0.160g (56.24%). Solubility: DMSO. M.P.: 280°C

In all above procedures for ligand synthesis, pure ligands were obtained. Also, the transition metal ions are known to facilitate the Schiff base formation reactions due to polarization and hence, can help in improving the yields. Hence, the following one pot methods for the synthesis of their complexes have been followed.

5.2.3 Synthesis of the binuclear copper complexes (C13-C16)

Complex **C13** **(**$[Cu_2(L^{13})(OAc)]\cdot H_2O$): 2,6-bis(aminomethyl)-4-nitrophenol dihydrochloride (0.270g, 1mmol) was suspended in methanol (10ml) and treated with a methanolic solution (10ml) of potassium hydroxide (0.112g, 2mmol). The resulting solution was allowed to reflux for 15 mins. After 15 mins, the resulting suspension (precipitated potassium chloride) was filtered and the filtrate was added dropwise to the hot methanolic solution (5ml) of 1-hydroxy-2-acetonaphthone (0.3724g, 2mmol) in a RB flask. The mixture was allowed to reflux for 5 hours. A hot methanolic solution (10ml) of $Cu(OAc)_2\cdot H_2O$ (0.399g, 2mmol) was added to ligand solution and the resulting solution was allowed to reflux for 3 hrs. The resulting dark green colour microcrystalline solid precipitates out within few hours of reaction. The product was filtered and washed with several times with cold methanol till the filtrate showed absence of any traces of impurities in TLC. Yield: 0.256g (34.88%). Solubility: DMSO, DMF.

Complex **C14** **(**$[Cu_2(L^{14})(OAc)]\cdot H_2O$): The procedure for the synthesis was analogous to the synthesis of ligand **C13** except using 2-hydroxy-1-acetonaphthone (0.3724g, 2mmol) in place of 1-hydroxy-2-acetonaphthone. The mixture was allowed to reflux for 3 hours. A hot methanolic solution (10ml) of $Cu(OAc)_2\cdot H_2O$ (0.399g, 2mmol) was added to ligand solution and the resulting solution was allowed to reflux for 3 hrs. The resultant dark green colour microcrystalline solid precipitates out within few hours of reaction. the solid was filtered and washed several times with cold methanol to remove traces of ligand and any impurities (TLC). Yield: 0.168g (22.89%). Solubility: DMSO, DMF.

Complex **C15 (**$[Cu_2(L^{15})_2](OAc)_2$): The procedure for the synthesis was analogous to the synthesis of ligand **C13** except using 2-formylpyrrole (0.1902g, 2mmol) in place of 1-hydroxy-2-acetonaphthone. The mixture was allowed to reflux for 4 hours. A hot methanolic solution (10ml) of $Cu(OAc)_2 \cdot H_2O$ (0.399g, 2mmol) was added to ligand solution and the resulting solution was allowed to reflux for 3 hrs. A dark greenish brown colour microcrystalline product precipitates out within few hours of reaction. The solid was filtered and washed several times with cold methanol to remove traces of ligand and any impurities (TLC). Yield: 0.452g (47.83%). Solubility: DMSO, DMF.

Complex **C16 (**$[Cu_2(L^{16})(OAc)] \cdot H_2O$): The procedure for the synthesis was analogous to the synthesis of ligand **C13** except using 8-formyl-7-hydroxy-4-methyl coumarin (0.408g, 2mmol) in place of 1-hydroxy-2-acetonaphthone. The mixture was allowed to reflux for 2 hours. A hot methanolic solution (10ml) of $Cu(OAc)_2 \cdot H_2O$ (0.3993g, 2mmol) was added to ligand solution and the resulting solution was allowed to reflux for 2 hrs. A dark green colour microcrystalline solid precipitates out within few hours of reaction. The product was filtered and washed several times with cold methanol to remove traces of ligand and any impurities (TLC). Yield: 0.607g (80.4%). Solubility: DMSO, DMF.

5.2.4 SOD mimic activity

The superoxide dismutase (SOD) activity was measured by using non-enzymatic method[6–9] (NADH-PMS-NBT assay) (**Scheme 2.2.4.1**) as explained in **section 2.2.4** of chapter 2.

5.2.5 Ascorbic Acid Oxidase (AAO) activity

Ascorbic Acid Oxidase (AAO) activity of all synthesized complexes has been evaluated by carrying out reactions of the complexes as catalysts with ascorbic acid as substrate wherein three different parameters such as substrate concentration, catalyst concentration and temperature have been varied. The concentration and temperature employed for this activity are mentioned below in a tabular form (**Table 5.2.5.1**).

The reaction rates, order and activation energy of reactions were calculated as explained in **section 2.2.4** in chapter 2. The ascorbate oxidase activity of all four complexes were studied by treating 2 x 10^{-6} M complex solution with 1 x 10^{-4} M

aqueous ascorbic acid solution under aerobic condition at 30°C. The time dependent wavelength scan was performed in acetate buffer medium (pH 5.5) to understand the potential of all complexes as catalyst towards the oxidation of ascorbic acid. The kinetic study of all these reactions was performed using initial rate method.

Table 5.2.5.1 *Concentration of ascorbic acid and catalyst with different parameters employed in this study*

Parameters	Concentration(mM)/Temp (°C)							
C13								
Ascorbic acid	[Cat=0.002mM and Temp= 30°C]							
	0.16	0.14	0.12	0.10	0.08	0.06	0.04	0.02
Catalyst	[Sub=0.1mM and Temp= 30°C]							
	0.001	0.002		0.003		0.004		0.005
Temperature	[Sub=0.1mM and Cat=0.002mM]							
	30	35		40		45		50
C14								
Ascorbic acid	[Cat=0.002mM and Temp= 30°C]							
	0.02	0.04	0.06	0.08	0.1	0.12	0.14	0.16	0.18
Catalyst	[Sub=0.1mM and Temp= 30°C]							
	0.001	0.002		0.003		0.004		0.005
Temperature	[Sub=0.1mM and Cat=0.002mM]							
	30	35		40		45		50
C15								
Ascorbic acid	[Cat=0.002mM and Temp= 30°C]							
	0.02	0.04	0.06	0.08	0.1	0.12	0.14	0.16
Catalyst	[Sub=0.1mM and Temp= 30°C]							
	0.001	0.002		0.003		0.004		0.005
Temperature	[Sub=0.1mM and Cat=0.002mM]							
	30	35		40		45		50
C16								
Ascorbic acid	[Cat=0.002mM and Temp= 30°C]							
	0.02	0.04	0.06	0.08	0.1	0.12	0.14	0.16
Catalyst	[Sub=0.1mM and Temp= 30°C]							
	0.002	0.003		0.004		0.005		0.006
Temperature	[Sub=0.1mM and Cat=0.002mM]							
	30	35		40		45		50

5.2.6 Catecholase activity

Catecholase activity of all four synthesized complexes has been evaluated by kinetic studies wherein three different parameters such as substrate concentration, catalyst

concentration and temperature have been varied. The concentration and temperature employed in this activity are summarized in **Table 5.2.6.1**.

The reaction rates, order and activation energy of reactions were calculated as explained in **section 2.2.6** in chapter 2. The kinetic study of the oxidation of catechol in presence of the complexes as catalysts involved initial rate method.

Table 5.2.6.1 *Temperature & Concentration of substrate and catalyst employed in this study*

Parameters		Concentration(mM)/Temp (°C)					
C13							
3,5-DTBC	**Substrate**	[Cat=0.04mM and Temp= 30°C]					
		1	2	3	4	6	8
	Catalyst	[Sub=4 mM and Temp= 30°C]					
		0.01	0.02	0.03	0.04	0.05	
	Temperature	[Sub=4 mM and Cat=0.04 mM]					
		30	35	40	45	50	
4-MC	**Substrate**	[Cat=0.04mM and Temp= 30°C]					
		2	4	6	8	10	
	Catalyst	[Sub=4 mM and Temp= 30°C]					
		0.01	0.02	0.03	0.04	0.06	
	Temperature	[Sub=4 mM and Cat=0.04 mM]					
		30	35	40	45	50	
C14							
3,5-DTBC	**Substrate**	[Cat=0.04mM and Temp= 30°C]					
		2	4	6	8	10	
	Catalyst	[Sub=4 mM and Temp= 30°C]					
		0.01	0.02	0.06	0.08		
	Temperature	[Sub=4 mM and Cat=0.04 mM]					
		30	35	40	45	50	
C15							
3,5-DTBC	**Substrate**	[Cat=0.04mM and Temp= 30°C]					
		2	4	6	8	10	
	Catalyst	[Sub=4 mM and Temp= 30°C]					
		0.01	0.02	0.06	0.08		
	Temperature	[Sub=4 mM and Cat=0.04 mM]					
		30	35	40	45	50	

5.2.5 Physical Measurements

5.2.5.1 Infrared studies

Infrared Spectra (4000-400 cm^{-1}) were recorded in the form of KBr pellets at 27°C using Perkin Elmer RX1 FTIR spectrometer and Bruker Alpha Transmission FT-IR spectrometer.

5.2.5.2 NMR studies

The ^{1}H NMR spectra of all synthesized ligand were recorded on Bruker Avance (400 MHz) NMR spectrometer in DMSO-d_6.

5.2.5.3 Mass studies

ESI-Mass of all complexes and ligands were recorded using XEVO G2-XS QTOF from IIT Ropar.

5.2.5.4 Electronic studies

Electronic spectra (200–900 nm) were recorded in methanol or DMSO or aqueous solutions using PerkinElmer UV-Vis spectrophotometer Model Lamda 35.

5.2.5.5 Photoluminescence studies

The emission spectra of all synthesized ligands and complexes were recorded on FP-6300 spectrofluorophotometer.

5.2.5.6 Elemental Analysis

Elemental analysis of synthesized complexes was recorded using EuroVector EA 300 at SAIF CDRI Lucknow.

5.2.5.7 ESR studies

ESR of all complexes were recorded using ESR JEOL using X- band frequency with 9.45 GHz and Bruker Biospin GmBH EPR instrument with a center field of 3200G using a microwave frequency in the range of 9.45 GHz in solid at RT and solution phase at LNT.

5.2.5.8 Molecular modelling

Molecular modelling has been used as a tool to get insights into the electronic structure of the complexes. The geometry of the complexes was optimized using GAUSSIAN 16 software program[10]. The calculations to find the ground state geometries were performed using B3LYP method[11] with 6-31G and LANL2DZ

basis sets[12,13]. Frontier molecular orbitals, HOMO (highest occupied molecular orbital) and LUMO (lowest unoccupied molecular orbital) have been visualized in Gauss View 6[14] and their energies have been calculated.

5.3 Results and Discussion

5.3.1 Characterization of ligands

5.3.1.1 IR spectroscopy

The IR spectra of ligands **L^{13}-L^{16}** consist of all important bands corresponding to the stretching and bending vibrations corresponding to the aliphatic and aromatic C-H, C-C, C-O of phenol, -NO_2 observed at their respective values as excepted for the ligands. The $\nu_{C=N}$ stretching frequency of ligand (**L^{13}-L^{16}**) appears in the range 1645-1590cm^{-1}. A band appears at around 3210.72cm^{-1} corresponding to -NH of pyrrole in the ligand **L^{16}**. A band corresponding to -C=O of cyclic ester in ligand **L^{16}** appears at around 1731.12cm^{-1} (See SI †: **Fig. S5.1-S5.4**). Some important frequencies are tabulated (**Table 5.3.2.1.1**).

Table 5.3.2.1.1 *IR frequencies of* ***L^{13}-L^{16}***

Ligands	$\nu_{C=N}$	ν_{N-H}	$\nu_{C=O}$ (cyclic ester)	ν_{O-H}
L_{13}	1615, 1590	-	-	3426.27
L_{14}	1616.32	-	-	3439.15
L_{15}	1631	3210.72	-	3400
L_{16}	1643.16	-	1731.12	3406.96

5.3.1.2 NMR Spectroscopy

The chemical shift values observed in the ^{1}H NMR spectra of ligands along with their splitting and assignment to specific protons are listed below. They are all consistent with the structures assigned to the ligands as shown in **Scheme 5.1.3** and support their formation.

Ligand **L^{13}:** ^{1}H NMR (δ ppm in DMSO-d_6): 2.628 (s, 3H, -C**H**$_3$), 2.618 (s, 3H, -C**H**$_3$), 3.863 (s, 2H, -C**H**$_2$-CH(OH)-CH$_2$-), 4.657-4.633 (aliphatic C-H), 6.702-8.317 (aromatic C-H), 15.793 (s, 2H, Ar-OH) (see SI†: **Fig. S5.5**).

Ligand **L^{14}:** ^{1}H NMR (δ ppm in DMSO-d_6): 2.309 (s, 6H, -C**H**$_3$), 3.385-4.615 (aliphatic C-H), 7.188-8.082 (aromatic C-H) (see SI†: **Fig. S5.6**).

Ligand **L^{15}:** ^{1}H NMR (δ ppm in DMSO-d_6): 3.383, 4.473-4.436 (m, 4H, methylene proton), 6.11-8.172 (pyrrole ring) 8.395 (s,2H, **H**-C=N), 11.647(s,2H, pyrrole NH) (see SI†: **Fig. S5.7**).

Ligand **L^{16}**: The NMR spectrum of **L_{16}** could not be recorded as it has very less solubility in suitable solvents.

5.3.1.3 Electronic spectra

The electronic absorption spectra of ligands (**L^{13}-L^{16}**) have been recorded (**Figure 5.3.1.3.1**). The observed wavelengths for π→π* and n→π* transitions are tabulated in **Table 5.3.2.3.1**.

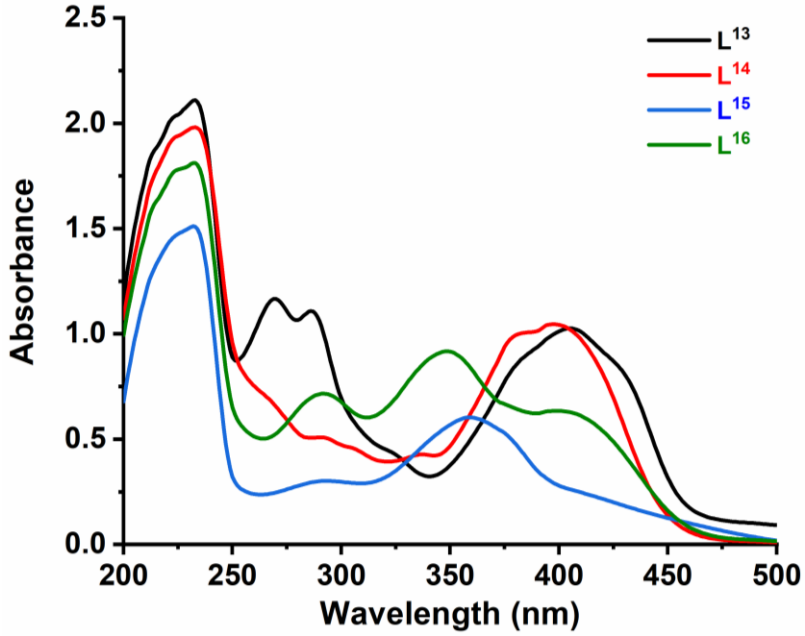

Figure 5.3.1.3.1 *UV-Vis spectra of* ***L^{13}-L^{16}*** *ligands*

5.3.1.4 Photoluminescence spectra

The ligands, **L^{13}** and **L^{16}** have fluorescent emission while **L^{14}** and **L^{15}** are not fluorescent. The emission band was observed at 521nm when a solution of ligand **L^{13}** was excited at λ_{max} = 405 nm. Similarly, an emission band was observed at 487 nm when a solution of ligand **L^{16}** was excited at λ_{max} = 400 nm. No fluorescent emission was observed when solutions of ligands **L^{14}** and **L^{15}** were excited in the region of their n→π* transitions at λ_{max} = 395 nm and 360nm, respectively. (**Figure 5.3.2.5.1**).

5.3.1.5. Mass Spectra

In the mass spectra of two isomeric ligands, $\mathbf{L^{13}}$ and $\mathbf{L^{14}}$, a peak is observed at *m/z*= 534.2033 and 534.2029 corresponding to $[M+H]^+$ where M= molecular weight of $\mathbf{L^{13}}$ and $\mathbf{L^{14}}$ = 533. (See SI† **Fig. S5.8-S5.9**) In the mass spectrum of ligand $\mathbf{L_{15}}$, a peak is observed at *m/z*= 352.1400 corresponding to $[M+H]^+$ where M= molecular weight of $\mathbf{L^{15}}$ = 351 (See SI† **Fig. S5.10**). In the mass spectrum of ligand $\mathbf{L^{16}}$, a peak is observed at *m/z*= 570.1503 corresponding to $[M+H]^+$ where M= molecular weight of $\mathbf{L^{16}}$ = 569 (See SI† **Fig. S5.11**). Thus, the mass spectra support the formation of the binucleating ligands.

5.3.2 Characterization of complexes

5.3.2.1 Elemental analysis

The elemental analyses of the complexes are consistent with the proposed formulae. The observed percentage of C, H and N present in the complexes are within the permissible limits of the values calculated from the empirical formula. The observed and calculated values are summarized in **Table 5.3.2.1.1**.

Table 5.3.2.1.1** Elemental analysis of complexes **C13 – C16

Complex	Empirical formula (M.W.)	%C	%H	%N
C13	$Cu_2C_{34}H_{27}O_7N_3{\cdot}H_2O$ (M.W.= 734)	55.669 (55.585)	4.074 (3.951)	5.937 (5.722)
C14	$Cu_2C_{34}H_{27}O_7N_3{\cdot}H_2O$ (M.W.=734)	55.129 (55.585)	3.871 (3.951)	5.645 (5.722)
C15	$Cu_2C_{40}H_{38}O_{10}N_{10}{\cdot}2H_2O$ (M.W.= 981)	49.012 (48.930)	4.191 (4.281)	14.324 (14.271)
C16	$Cu_2C_{32}H_{23}O_{11}N_3{\cdot}H_2O$ (M.W.=770)	49.148 (49.870)	3.168 (3.247)	5.287 (5.455)

** The values in parentheses are calculated from the formula in column 2 of the table.*

5.3.2.2 IR spectra

In the IR spectra of complexes **C13-C16**, $\nu_{C=N}$ appears at around 1630-1615cm^{-1} (see SI†: **Fig S5.12-5.15**). The $\nu_{C=N}$ stretching in all complexes have shifted to a lower frequency as compared to that in the free ligand, clearly indicating the participation of imine N in coordination with copper ion (**Table 5.3.2.2.1**).

Table 5.3.2.2.1 *IR frequencies of complexes* **C13-C16**

Complex	$\nu_{C=N}$ (cm^{-1})	$\nu_{C=O}$ (cm^{-1})	ν_{N-H} (cm^{-1})	ν_{O-H} of water (cm^{-1})
C13	1617.33	-	-	3447.84
C14	1615.21	-	-	3442.49
C15	1631.96	-	3357.21	3443.64
C16	1626.52	1726.46	-	3435.43

A band appears at 3357.21cm^{-1} corresponding to N-H of pyrrole ring in **C15**. A band appears at around 1731.12cm^{-1} corresponding to -C=O of acetyl group in free ligand $\mathbf{L^{16}}$ while that in complex **C16** appears at 1726.46cm^{-1}. The peak at 3400-3500 cm^{-1} corresponds to the νO-H of water molecules (coordinated or present in the lattice) in complexes (**C13-C14**).

5.3.2.3 Mass spectra

In the mass spectrum of complex **C13**, a peak was observed at *m/z* = 534.2108 due to $[L^{13}+H]^+$ (Mol wt. = 533). A very distinct combination of peaks of isotopic masses corresponding to the $[Cu_2(L^{13})(CH_3COO)(H_2O)+2H^+]^{2+}$ (FW = 367.5) is observed at *m/z*= 366.1505 - 369.1650. The peaks was observed at *m/z*= 597.1257 and 678 may be assigned to the complex fragments $[[Cu(L^{13})]+H]^+$ and $[Cu_2(L^{13})H_2O+H]^+$.

A similar pattern has been observed in the mass spectrum of the isomeric complex **C14.** A peak was observed at *m/z* = 534.2106 due to $[L^{14}+H]^+$ (Mol wt. = 533). A very distinct combination of peaks of isotopic masses corresponding to the $[Cu_2(L^{14})(CH_3COO)(H_2O)+2H^+]^{2+}$ (FW = 367.5) is observed at *m/z*= 366.1511 - 369.1648. The peaks was observed at *m/z*= 595.1248, 597.1248 can be assigned to the fragment $[[Cu(L^{14})]+H]^+$.

In the mass spectrum of complex **C15**, a peak was observed at *m/z*= 352.1454 due to $[(L^{15}+H]^+$ (Mol wt. = 351). A combination of peaks observed between *m/z* = 253.9295 – 258.0911 corresponds to the isotopic masses of the molecular fragment $[[Cu(L^{15})(OAc)(H_2O)_2+2H^+]^{2+}$ (FW = 254). Another distinct combination of peaks observed at *m/z*= 491.3069 and 492.3103 is due to the molecular dication $[[Cu_2(L^{15})_2(OAc)_2(H_2O)_2+2H^+]^{2+}$ or $[[Cu(L^{15})(OAc)(H_2O)+H^+]_2^{2+}$. The appearance of these two peaks is a confirmation of the formation of a dimer rather than a

monomer as the latter would have distinct isotopic masses differing by 2 units corresponding to the major isotopes of copper with mass numbers 63 and 65. Another distinct peak combination observed at 717.4783, 718.4810 and 719.4802 is due to the loss of a major fragment (*m/z*= 263) from the molecule (980 – 263 = 717).

In the mass spectrum of complex **C16**, the peak observed at *m/z*= 631.0743 corresponds to $[Cu(L^{16})]^+$ (FW = 630). The peak was observed at *m/z*= 772.0029 corresponds to the protonated complex molecule, $[[Cu_2(L^{16})(OAc)]\cdot H_2O+H^+]^+$ (Mol wt = 771). (see SI†: **Fig S5.16-5.19**).

5.3.2.4 Electronic spectroscopy

The wavelengths of absorption with molar absorptivity values of the bands observed in the electronic spectra of the ligands, $\mathbf{L^{13}}$-$\mathbf{L^{16}}$, and complexes, **C13-C16**, have been listed in **Table 5.3.2.4.1**.

The electronic absorption spectra of the complexes, **C13-C16**, have a charge transfer band appearing at λ_{max} = 340 - 400 nm which may be assigned to MLCT transition in the complexes. This becomes possible due to the involvement of the ligand in π-interaction with the metal ion. All complexes have a weak ligand field band in the range of 610-670nm in the visible region which is characteristic of highly distorted geometry around copper centres. The intra-ligand, π→π* and n→π* transitions appear between at around 200-370nm in all complexes.

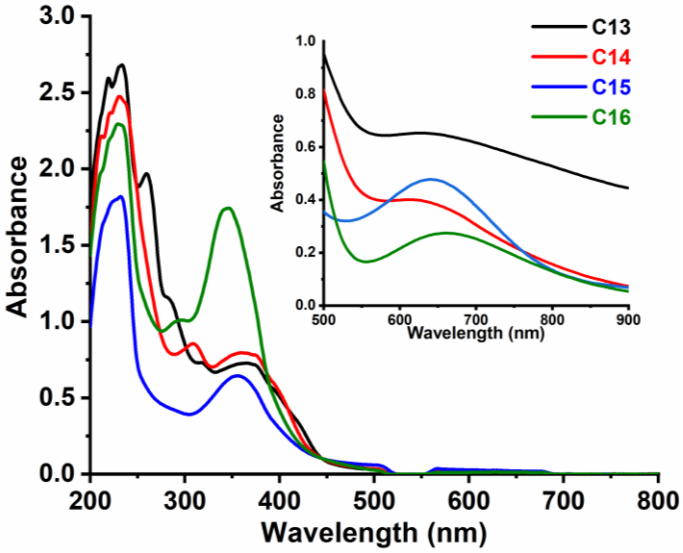

Figure 5.3.2.4.1 *UV-Vis spectra of complexes,* ***C13-C16***

The intense higher energy band in the range of 200-300 nm is due to intra ligand π-π* and in case of ligands in the range of 300-460nm is due to n-π* transitions (**Figure 5.3.2.4.1**).

Table 5.3.2.4.1 *Electronic spectra of ligands,* ***L^{13}-L^{16}*** *and complexes,* ***C13-C16***

Complexes	**λ_{max}/nm (ε_{max}/dm^{3}mol^{-1}cm^{-1})**		
	Intra-ligand transitions	Charge transfer	d-d transitions
L_{13}	233 (52750), 269(29250), 287(27750), 406(25500)	-	-
C13	232(66750), 259(49000), 361(18275)	399(13305)	630 (660)
L_{14}	233(49750), 288(12750), 384(25000), 397(26250)	-	-
C14	231(62250), 309(21800), 361(19625)	394(14940)	612(395)
L_{15}	232(37750), 295(7500), 359(15250)	-	-
C15	231(45250), 293(24670), 358(16100)	396(8075)	639(483)
L_{16}	231(45250), 292(18000), 349(23000), 400(16000)	-	-
C16	231(57500), 293(25275), 344(43650)	391(13668)	663(277)

It is known that the transition $^2T_{2g} \leftarrow {}^2E_g$ in a d^9 system (in octahedral geometry), usually appears between 600 and 800 nm. On distortion from octahedral to distorted octahedral / square pyramidal / trigonal bipyramidal or square planar structure, this band undergoes a significant shift and broadening due to splitting of the spectral states and multiple transitions merging to form a broad band.[15] In the complexes **C13-C16**, it is observed to be very broad indicating a combination of several transitions becoming possible due to further splitting of the spectral states in a distorted, most probably square planar, geometry.

5.3.2.5 Photoluminescence spectra

The ligands **L^{13}**, **L^{16}** and their respective complexes, **C13** and **C16** are all fluorescent. When a solution of ligand **L^{13}** solution was excited at λ_{max} = 405 nm, an emission band was observed at 521nm. The complex **C13** gave fluorescent emission at 465 nm when its solution was excited at λ_{max} = 365nm. The complex has lower fluorescence intensity (**Figure 5.3.2.5.1**). An emission band was observed at 487 nm when a solution of ligand **L^{16}** was excited at λ_{max} = 400 nm. A similar emission band

was observed at 443nm when the solution of complex **C16** was excited at the same wavelength, λ_{max} = 400nm (**Figure 5.3.2.5.1**).

No emission band was observed when the solutions of ligands $\mathbf{L^{14}}$, $\mathbf{L^{15}}$ and their respective complexes **C14** and **C15** were excited in their 360 & 395 nm bands, respectively (**Figure 5.3.2.5.1**). That is these ligands and complexes do not exhibit fluorescence.

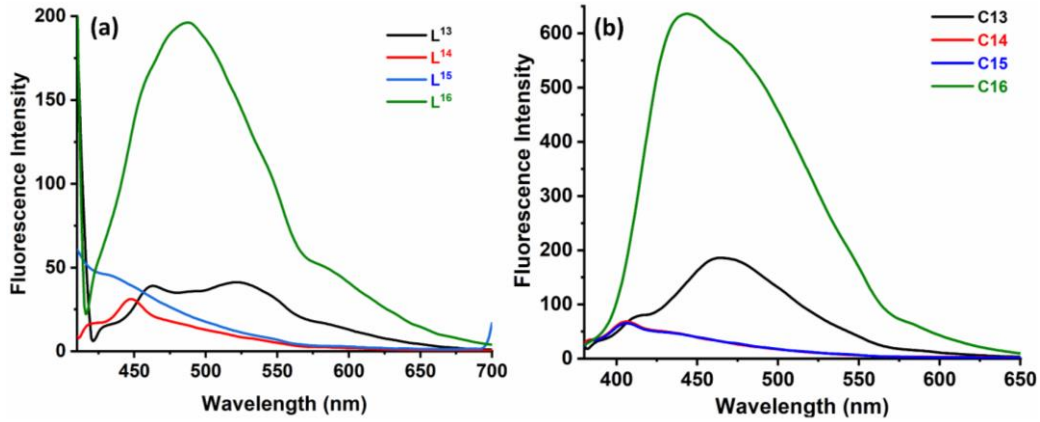

Figure 5.3.2.5.1 *Emission spectra of (a)* ***L^{13}, L^{14}, L^{15}*** *and* ***L^{16}*** *(b)* ***C13, C14, C15*** *and* ***C16***

5.3.2.6 ESR spectra

The ESR spectra of all complexes were recorded both in powder at RT and solution state at liquid nitrogen temperature (LNT). (**Table 5.3.2.6.1**).

Table 5.3.2.6.1 *g_{II}, $g_{\perp}$ and A_{II} or $A_{\perp}$ values of complexes,* ***C13-C14***

Complex	g_{II}	$g_{\perp}$	A_{II} /$A_{\perp}$x 10^{-4} cm^{-1}
C13	2.394	2.117	179/39.5
C14	EPR silent		

The ESR spectra of complexes recorded in the form of powdered solid samples at RT, indicate near axial field around the copper(II) centres. The spectrum of C13 in frozen solution at LNT consists of clear hyperfine splitting due to the coupling of electron spin with the nuclear spin of copper ions. The A_{II} value is typical of a moderately hard coordination environment. The complex **C14** is found to be EPR silent in DMSO solution at LNT. This indicates the presence of moderately strong

antiferromagnetic coupling between the copper(II) centers of the dicopper(II) complex (**Figure 5.3.2.6.1**).

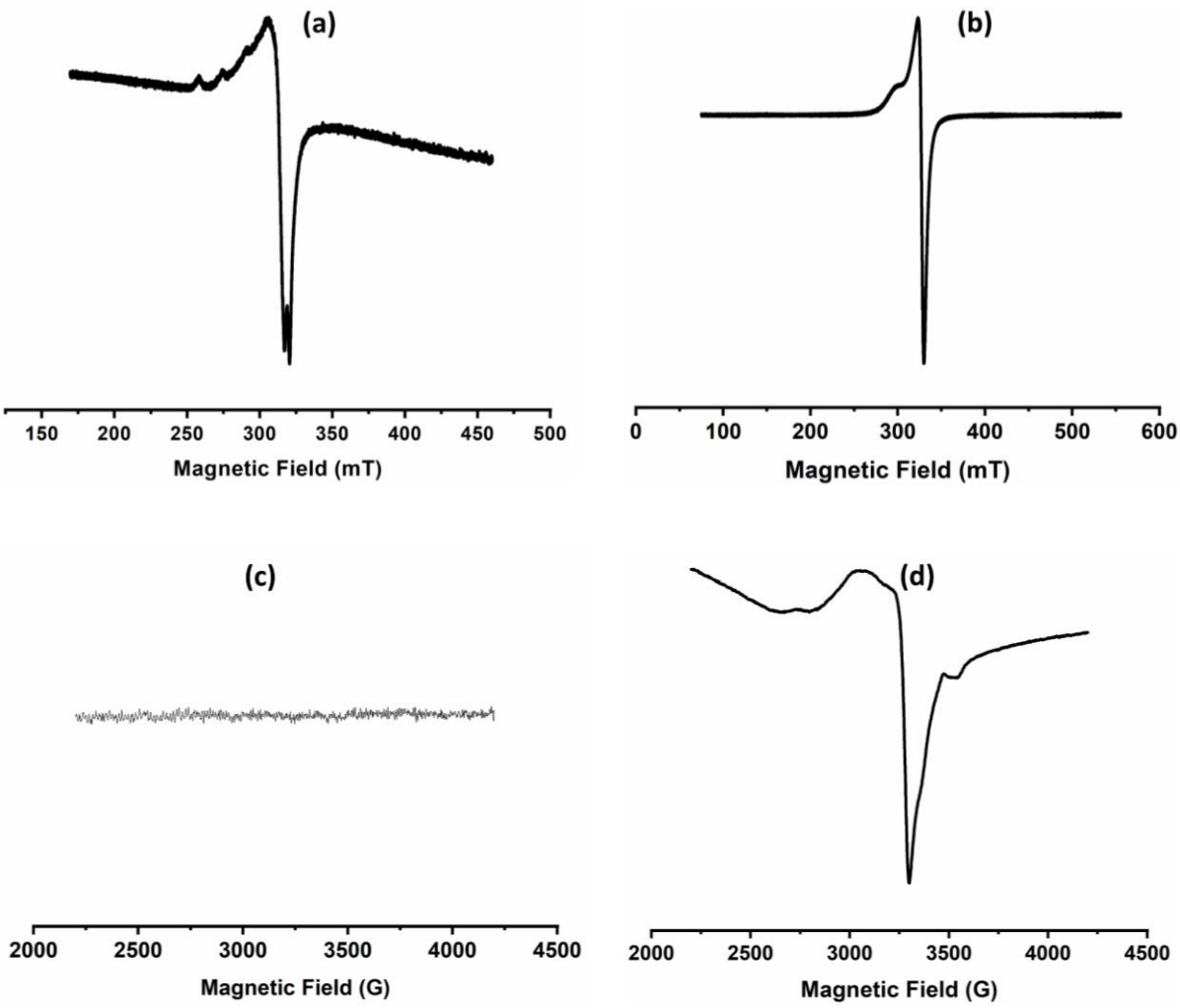

Figure 5.3.2.6.1 *ESR spectra of complexes (a)* ***C13****(DMSO)(LNT) (b)* ***C13*** *(powder)(RT) (c)* ***C14*** *(DMSO)(LNT) (d)* ***C14*** *(powder)(RT)*

5.3.2.7 Molecular Modelling

To get insight into the electronic structure, the geometrical parameters of complexes **C13-C14** were optimized in the gas phase using GAUSSIAN 16 program[10,12–14] with B3LYP and LANL2DZ basis set (**figure 5.3.2.7.1**). The calculated bond parameters are tabulated (see SI in **Table. S5.1**). Contour plots of HOMO and LUMO and the energy gap, ΔE_g, between them is shown in **figure 5.3.2.7.2**) which is expected to play an important role in deciding their enzyme mimic and other biological activity[16]. These frontier molecular orbitals, LUMO and HOMO act as electron acceptor and electron donor[17], respectively and influence the reactivity of the

molecule. Theoretically calculated transition energy between HOMO and LUMO in complexes, **C13-C16** are summarized in **Table 5.3.2.7.1**. These ΔE_g values also reflect upon the catalytic activity[18,19] of the complexes. The HOMO-LUMO energy gap (ΔE_g) in the complexes follow order **C13 < C16 < C14 < C15.** The ΔE_g value for complex **C13** is the lowest which is reflected in the highest SOD, catacholase mimic and ascorbic acid oxidase mimic activity of this complex as comparedto the remaining complexes considered here.[18,19]. **Figure 5.3.2.7.3** shows the graphical representations of ESP for complexes **C13-C16**.

Table 5.3.2.7.1 *Global reactivity descriptors of complexes in eV calculated by DFT/B3LYP/LANL2DZ basis set*

Molecular Properties	Mathematical Description	C13	C14	C15	C16
E_{HOMO}	Energy of HOMO	-5.1378	-5.5789	-5.5076	-5.9163
E_{LUMO}	Energy of LUMO	-4.4238	-4.7658	-4.0474	-4.9873
Energy gap	$\Delta E_g = E_{LUMO} - E_{HOMO}$	0.714	0.8131	1.4602	0.929
Ionization potential (IP)	$IP = -E_{HOMO}$	5.1378	5.5789	5.5076	5.9163
Electron Affinity (EA)	$EA = -E_{LUMO}$	4.4238	4.7658	4.0474	4.9873
Electronegativity (χ)	$\chi = -\frac{1}{2}(E_{HOMO} + E_{LUMO})$	4.7808	5.1724	4.7775	5.4518
Chemical Potential (μ)	$\mu = \frac{1}{2}(E_{HOMO} + E_{LUMO})$	-4.7808	-5.1724	-4.7775	-5.4518
Global Hardness (η)	$\eta = -\frac{1}{2}(E_{HOMO} - E_{LUMO})$	0.357	0.4066	0.7301	0.4645
Softness (S)	$S = 1/2\eta$	1.4005	1.2299	0.6848	1.0764
Electrophilicity index (ω)	$\omega = \mu^2/2\eta$	32.01	32.90	15.63	31.99

The energy gap (ΔE_g), E_{HOMO} and E_{LUMO} values are important for the prediction of global reactivity descriptors, which in details explains the internal charge transfer,

stability and reactivity of the molecule[19]. Global reactivity descriptors such as electronegativity (χ), global hardness (η), global electrophilicity (ω) and global softness (σ) are calculated using the formulas based on Koopmans theorem[20] (**equations 2.3** to **2.7** in chapter 2 **section 2.3.2.9**) (**Table 5.3.2.7.1**).

The optimized structures of all synthesized complexes (**C13-C16**) are depicted in **figure 5.3.2.7.1**. Each copper(II) ions are four coordinated in all complexes **C13-C16** except complex **C15**, each copper(II) ions are six coordinated. In all complexes, both copper ions are coordinated by alcoholic oxygen, imine nitrogen, phenoxo oxygen of acetonaphthones (complex **C13** & **C14**) or of coumarin unit (for complex **C16**) and imine nitrogen in complex **C15** of ligand **L**[15]. Besides these, some important geometrical parameters such as bond angles, bond lengths, torsion angle related to the complexes are tabulated in supplementary information (See SI† **Table S5.1**).

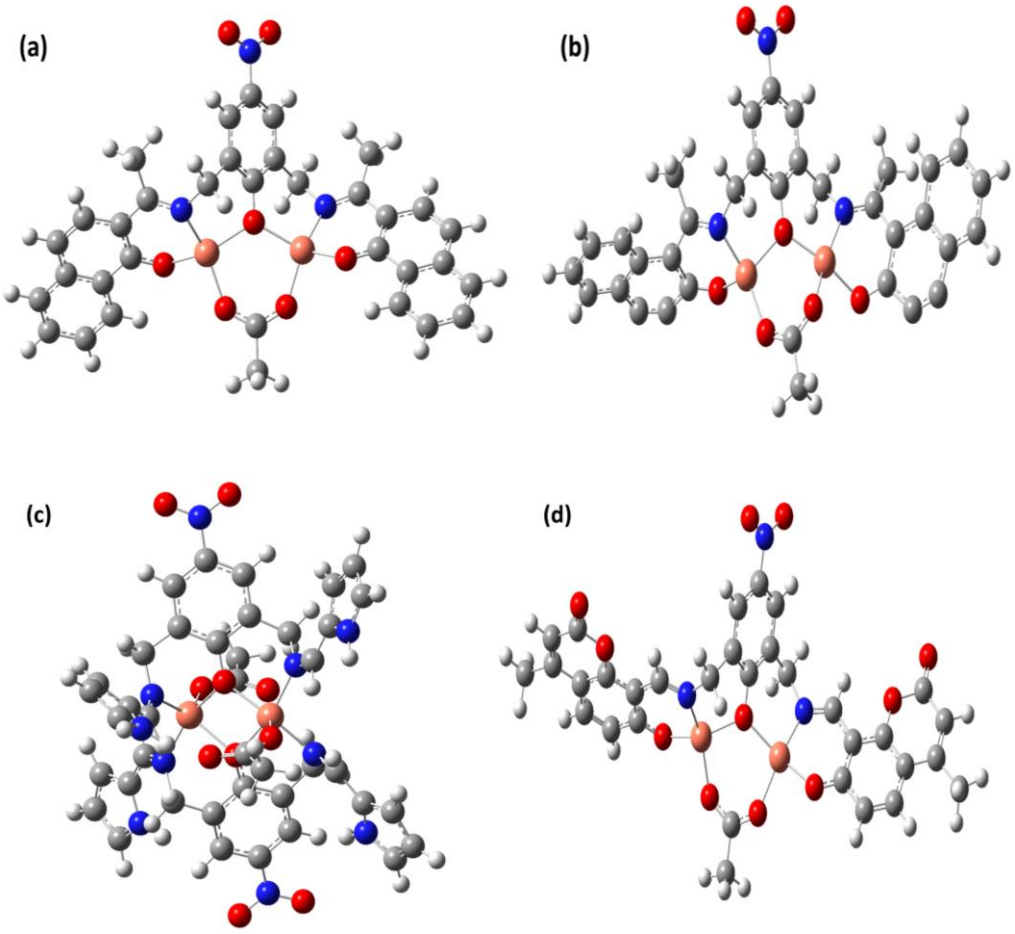

Figure 5.3.2.7.1 *DFT optimized structure of complexes (a)**C13** (b) **C14** (c) **C15** (d) **C16***

The calculated bond lengths of Cu-N and Cu-O of these complexes are comparable to those reported four coordinated complexes obtained from single crystal X-ray data. In all the complexes, HOMO and LUMO along with their two upper and two lower orbitals exhibits different localization indicating intramolecular electron charge transfer within the molecule. The energy gap (ΔE_g) value is directly associated with the stability and hardness and inversely related with the reactivity and softness of the molecule. A very small energy gap values shows that there is an easy charge transfer within the molecule, which may further increase the biological activity of the complex.

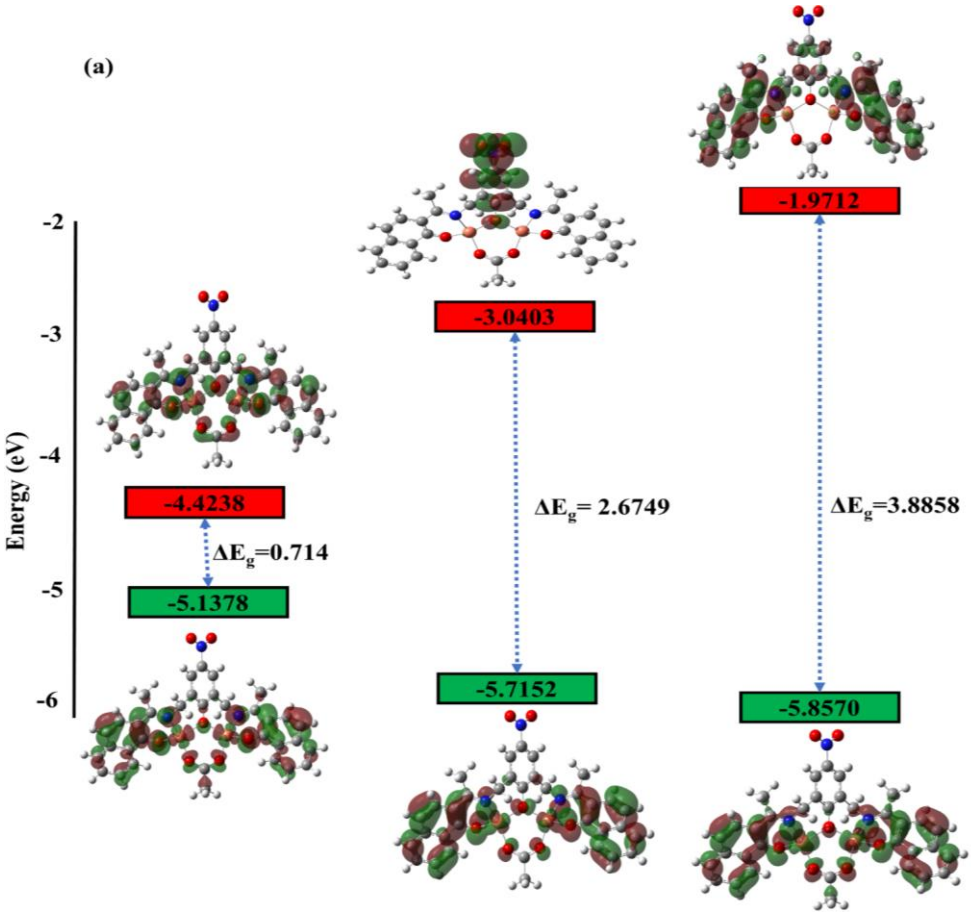

Figure 5.3.2.7.2 *(a) Frontier molecular orbitals of complex* ***C13***

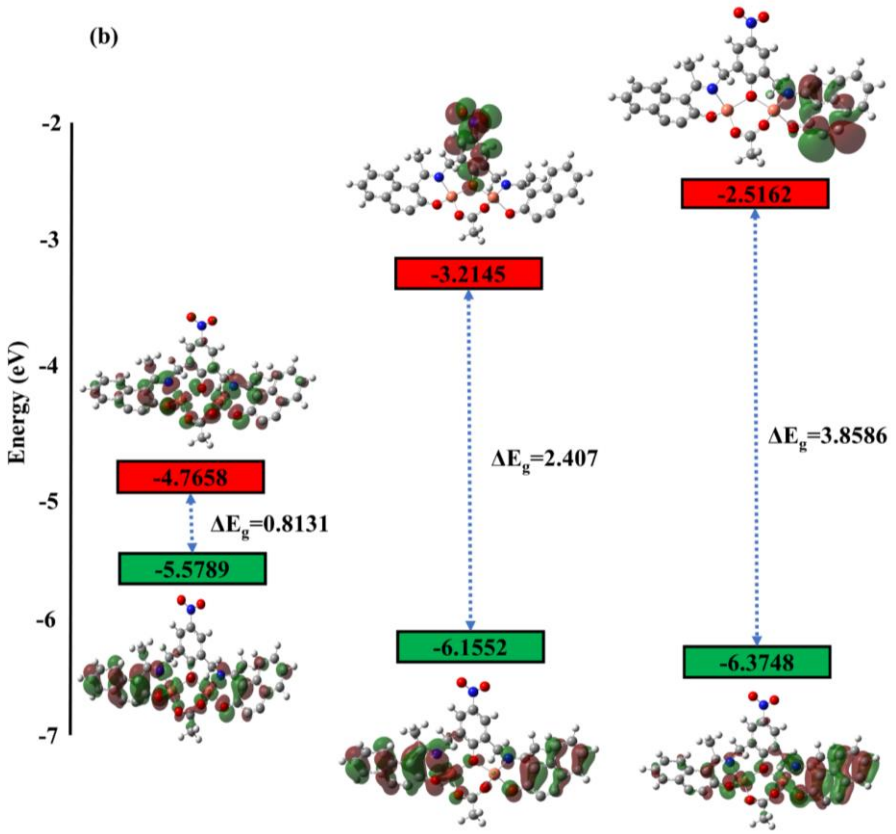

Figure 5.3.2.7.2 *(b) Frontier molecular orbitals of complex* ***C14***

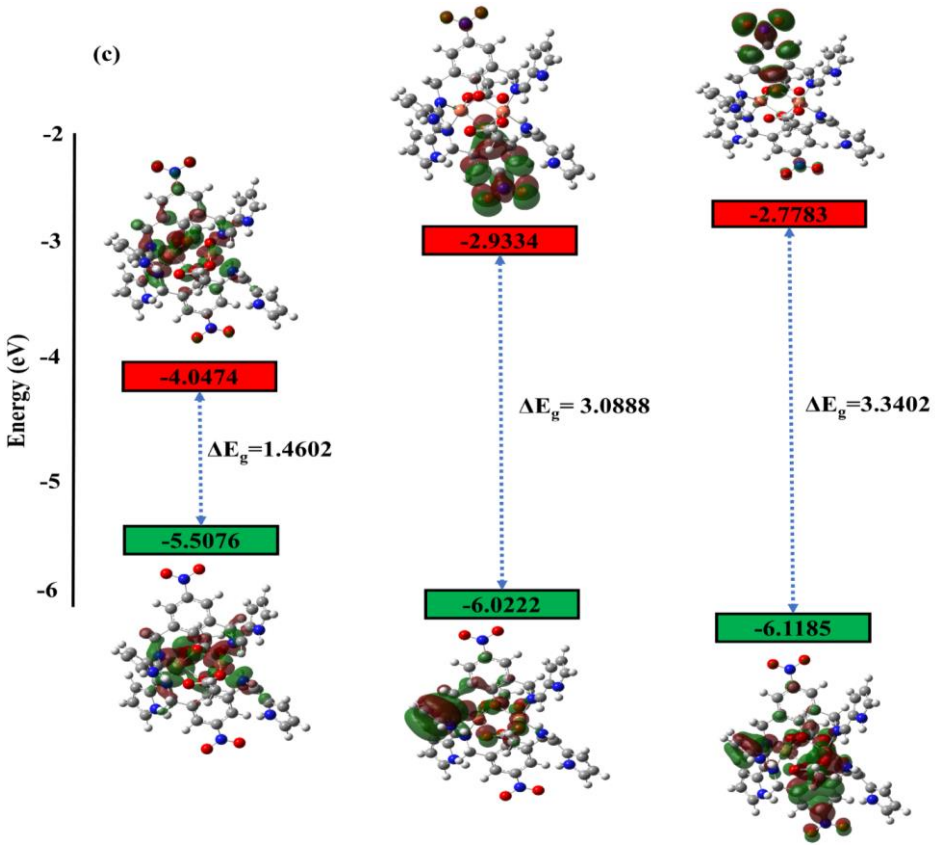

Figure 5.3.2.7.2 *(c) Frontier molecular orbitals of complex* ***C15***

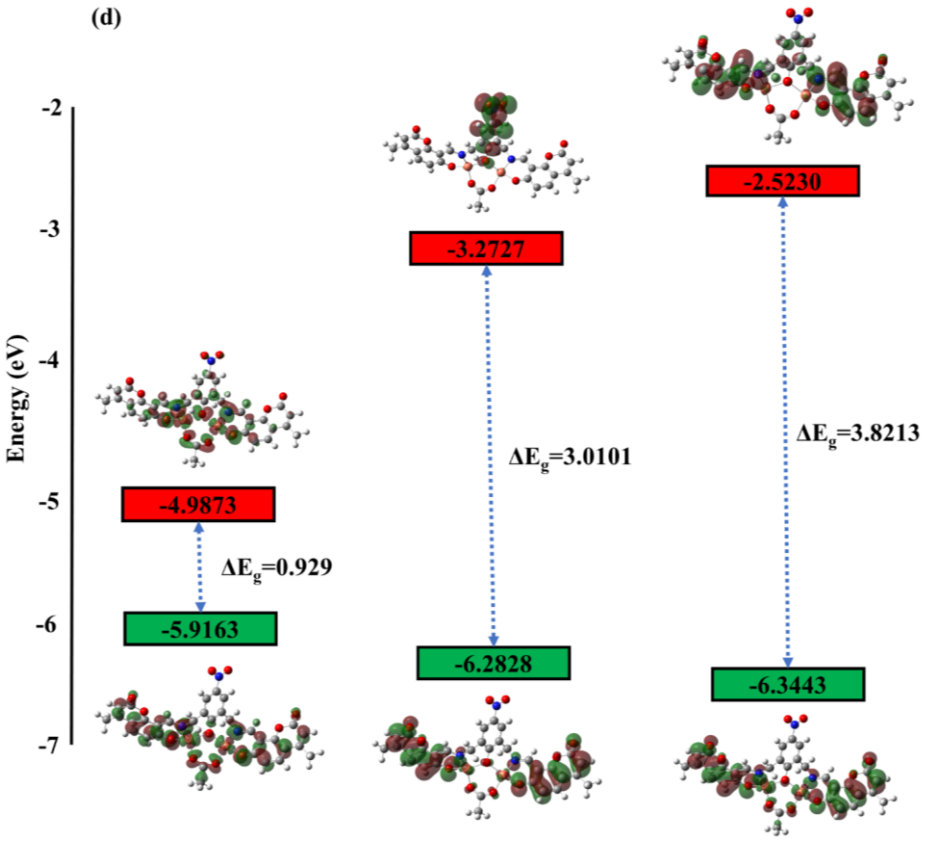

Figure 5.3.2.7.2 *(d) Frontier molecular orbitals of complex* ***C16***

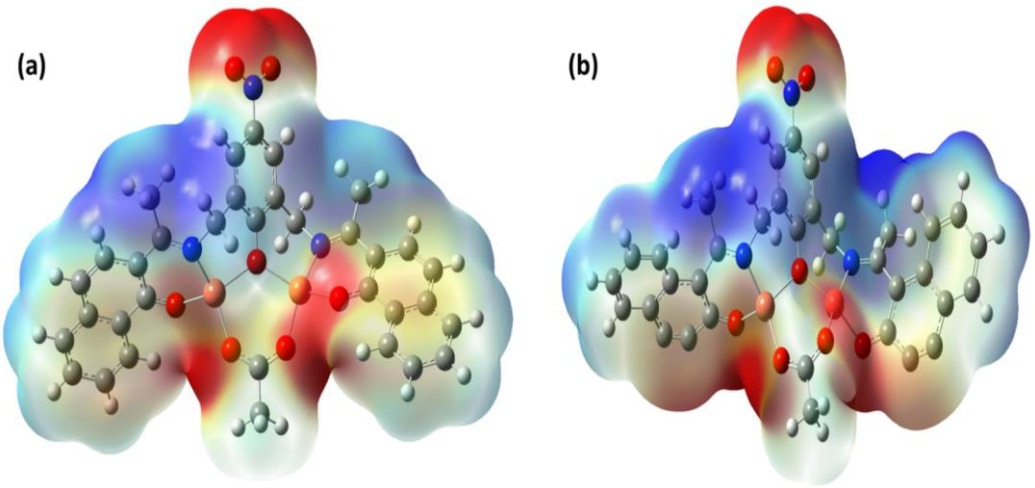

Figure 5.3.2.7.3 *Electrostatic potential of complexes (a)* ***C13*** *(b)* ***C14***

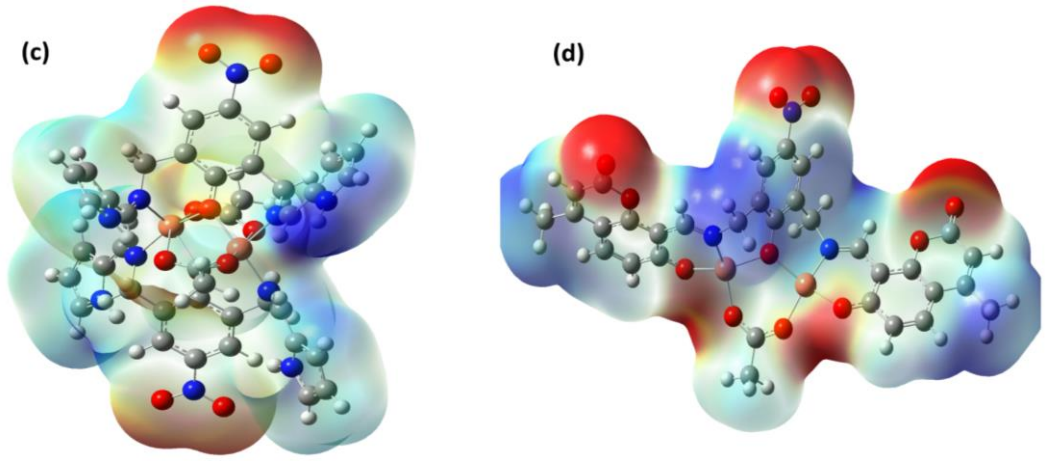

Figure 5.3.2.7.3 *(Contd…) Electrostatic potential of complexes (c)* ***C15*** *and (c)* ***C16***

5.3.3 SOD mimic activity of the complexes

Generation of superoxide anion ($O_2^{\cdot-}$) is responsible for the conversion of NBT to mono-formazan complex. The hydrogen donor NADH reduces PMS. This reduced PMS generates $O_2^{\cdot-}$ from dissolved O_2. NBT gets reduced by $O_2^{\cdot-}$, which results in a linear accumulation of blue formazan with increase in the absorbance at 560nm (**scheme 2.3.3.1** in chapter 2 **section 2.3.3**). Therefore, the scavenging of superoxide through any mechanism results in the decrease in the accumulation of the blue formazan and hence, lower absorbance at 560nm.

In the reaction medium, SOD or SOD mimic compounds scavenge $O_2^{\cdot-}$ which results in decrease in the formation of formazan. The % inhibition of NBT reduction at various concentrations of complexes as a function of time was measured by measuring the absorbance at 560nm. **Figure 5.3.3.1** represents the plot of absorbance (A_{560}) against time (t) with varying concentration of complexes required to yield the reduction of NBT. The NBT reduction value of complexes is higher than exhibited by the copper salts. All four ligands show very low % inhibition at 100µM concentration of ligand. The % inhibition of NBT reduction was found to be 20.30 %, 39.06%, 35.01% and 33.65%, respectively, for $\mathbf{L^{13}}$, $\mathbf{L^{14}}$, $\mathbf{L^{15}}$ and $\mathbf{L^{16}}$ at this concentration. This confirms that the ligands do not have good SOD mimicking activity. (**Figure 5.3.3.1 (d)**)

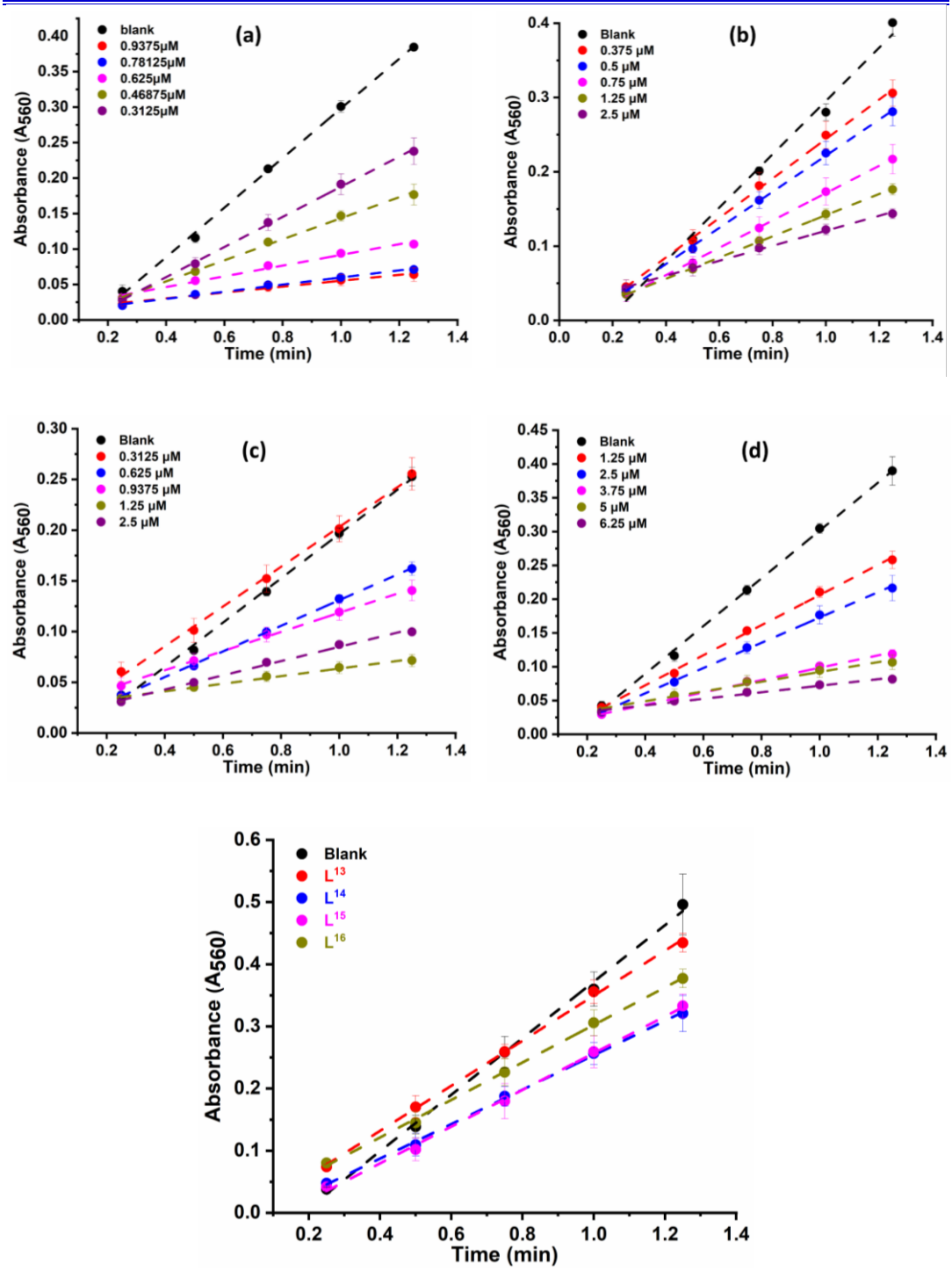

Figure 5.3.3.1 *Plot of Absorbance (A_{560}) as function of time (min) (a)* ***C 13*** *(b)* ***C14*** *(c)* ***C15*** *(d)* ***C16*** *and (e)* ***L^{13}-L^{16}***

Figure 5.3.3.2 represents % inhibition of NBT reduction as a function of increasing concentrations of complexes which is used for determining the IC_{50} value of each complex. The copper(II) complexes showed good SOD mimic activity, which was

evaluated by the scavenger concentration causing 50% inhibition of reduction of NBT, IC_{50}.

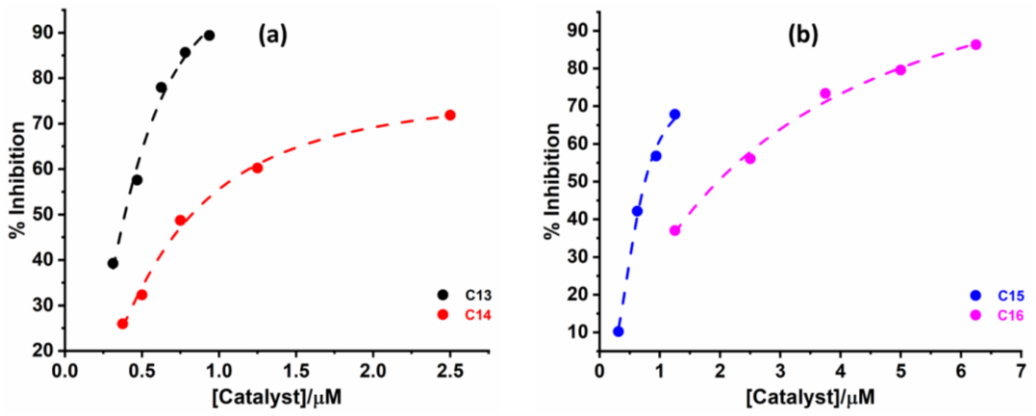

Figure 5.3.3.2 *Plot of % inhibition of NBT reduction vs. concentration of complexes (a)* ***C13 & C14*** *(b)* ***C15 & C16***

All four complexes exhibit SOD-like activity at the biological pH with IC_{50} values ranging between 0.385-1.923μM for binuclear copper(II) complexes. The complexes, **C13-C16**, show better SOD mimic activity than those reported in literature.[6,7,9,21–23]

Table 5.3.3.1 *IC_{50} values of ligands (**L^{13}-L^{16}**) & complexes **(C13-C16)** and of the native enzyme*

Complexes	IC_{50}/μM
L^{13}	>100
C13	0.385
L^{14}	>100
C14	0.925
L^{15}	>100
C15	0.794
L^{16}	>100
C16	1.923
Native enzyme (SOD)	0.04

The IC_{50} values summarized in **Table 5.3.3.1** further show that the complex C13 has highest activity with the lowest IC_{50} value of 0.385 and the activity decreases in the order **C13 > C15 > C14 > C16.** This order is same as that of the ionization potential values calculated for the optimized geometries. This is also similar to the order of HOMO-LUMO gap with an exception of **C15**, where LUMO has much higher energy and is not centred over the metal ions.

5.3.4 Ascorbic Acid Oxidase (AAO) activity

The oxidation of AA as catalyzed by complexes in dissolved O_2 in presence of acetate buffer (pH 5.5) was monitored by measuring absorbance at λ_{max} = 265nm using UV-Vis spectroscopy. A distinct absorption maximum at λ_{max} = 265nm (marked as 'a') was observed for ascorbic acid (AA) (**figure 5.3.4.1 (a)**). However, in presence of complexes under aerobic conditions, a significant decrease in the absorbance of AA (marked as 'b') was noted which demonstrated the fact that AA was consumed in a reaction (**figure 5.3.4.1 (a)**). When the same experiment was carried out under nitrogen atmosphere, there was no significant decrease in the absorbance at λ_{max} = 265nm (marked as 'c') which confirms the involvement of O_2 in the reaction (**Figure 5.3.4.1(a)**). When a similar experiment was carried out in presence of corresponding copper salts, there was a significant decrease in the absorbance at λ_{max} = 265nm (marked as 'd'), however, the reaction was stoichiometric rather than catalytic (**Figure 5.3.4.1 (a)**). The time dependent (0-40 mins) changes in the absorption spectra upon oxidation of AA by O_2 in the presence of complexes are depicted in **Figure 5.3.4.1(b)** for complex **C13** and in SI†: **Fig. S5.20A-C (a,e,g)** for other complexes. The absorbance band at λ_{max} = 265nm decreases with time from 0 min to 40 min and completely disappears after 40 min which confirms that complexes quickly catalyze the oxidation of AA to DHAA. Rate of reaction for all complexes was obtained by initial rate method by plotting [AA] as a function of time. The molar absorptivity of the ascorbic acid band was considered to be ε = 14500 $dm^3mol^{-1}cm^{-1}$. **Figure 5.3.4.1(c-e)** shows plot of [AA] as function of time for complex **C13** and for other complexes (SI†: **Fig. S5.20A-C (b-d,f-h,i-k)**). To obtain the steady-state kinetic parameters, we further studied the catalytic behaviour of complexes with AA as substrate, built on enzyme kinetics theory and methods. The most commonly and widely used models and methods to study the enzymatic reaction was Michaelis-Menten model. In **Figure 5.3.4.2**, the solid circles are experimental data and solid curves are the fits to the Michaelis-Menten model for all complexes.

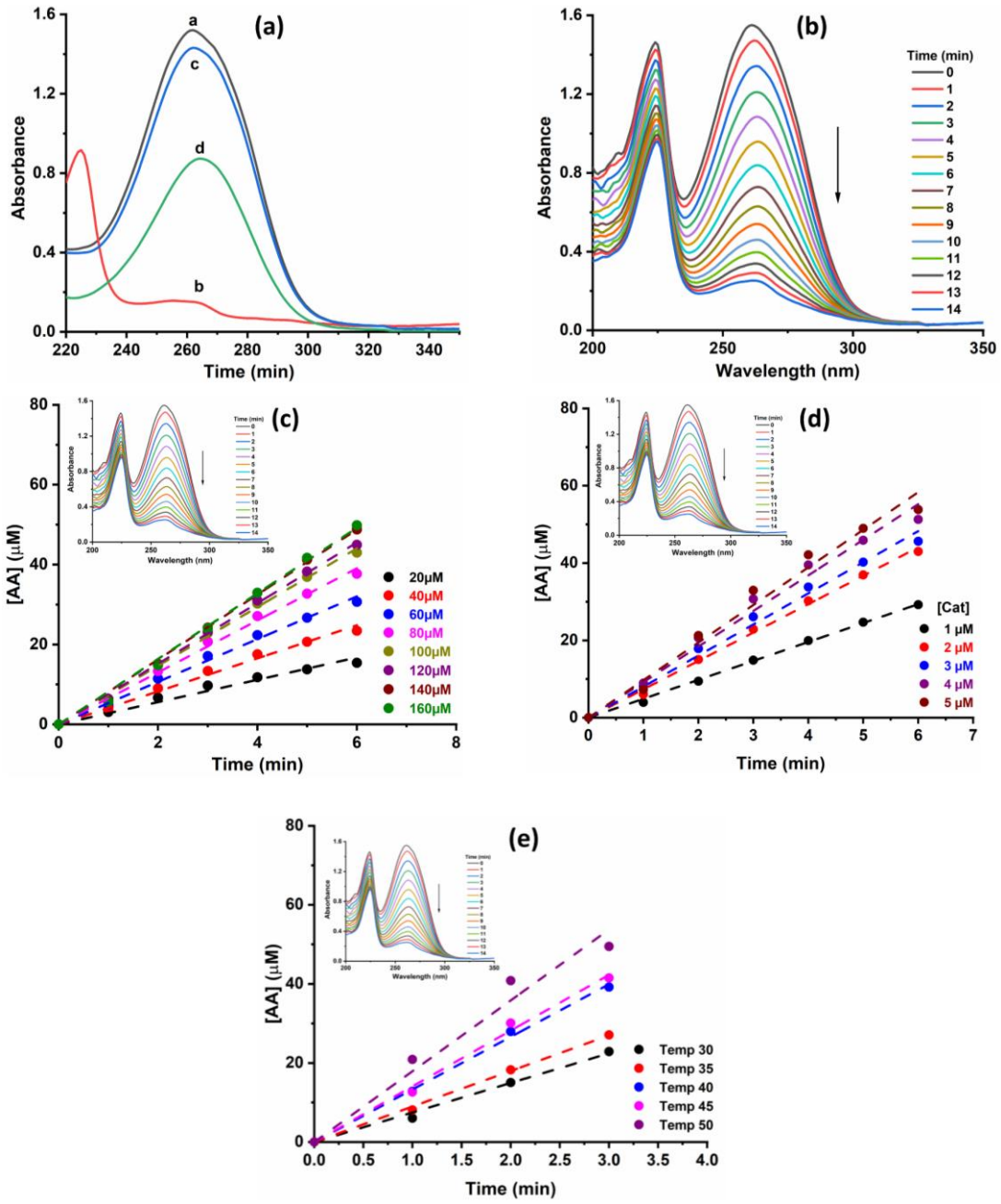

Figure 5.3.4.1 *(a) Uv-Vis spectra of a: AA, b: AA+**C13** under aerobic conditions, c: AA+**C13** under a N_2 atm. for 20 mins and d: AA+$Cu(OAc)_2$ for 20 mins under aerobic conditions,*

*(b) Time dependent spectral changes from 0 to 14 mins of AA corresponding to **C13** catalyzed oxidation and (c-e) Plot of [AA] as function of time w.r.t. substrate (c), catalyst (d) and temperature (e) (Inset: Plot of absorbance vs wavelength at different time interval)*

With various concentrations of ascorbic acid (AA), Michaelis-Menten constant (K_m) can be obtained from the Menten equation (**equation 2.8** in **section 2.3.4** in chapter 2). The Michealis-Menten constant (K_m) and maximum rate (V_{max}) can be calculated by Lineweaver-Burk plot. The kinetic of the reactions can be understood with the help of parameters K_m and catalytic rate (k_{cat}).

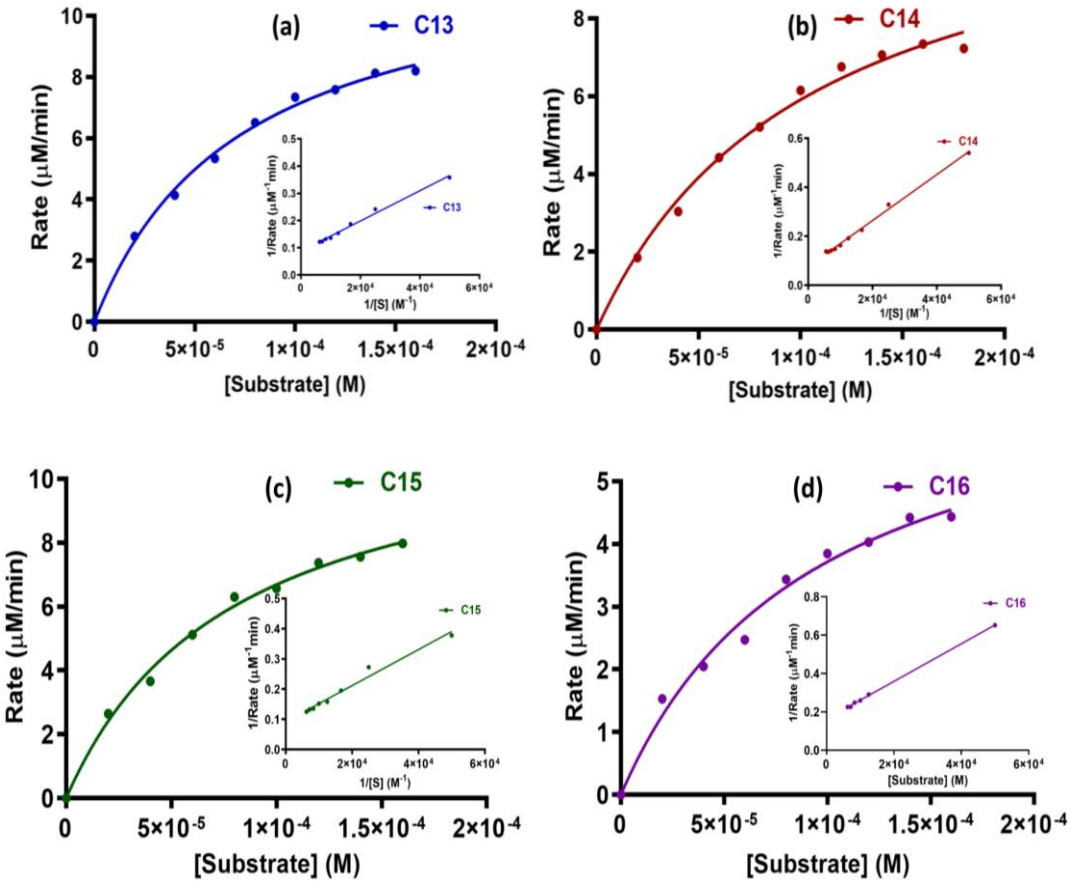

Figure 5.3.4.2 *Rate vs [substrate] plot of Michaelis menten model for complexes (a)* ***C13*** *(b)* ***C14*** *(c)* ***C15*** *and (d)* ***C16*** *(Inset: Lineweaver Burk plot of respective complexes)*

The order of reaction with respect to substrate was obtained from slope of the plot of log(rate) as function of log[substrate] (**Figure 5.3.4.3**), while order with respect to catalyst was obtained from slope of the plot of log(rate) as function of log[catalyst] (**Figure 5.3.4.4**). It was found to be half order with respect to substrate as well as catalyst.

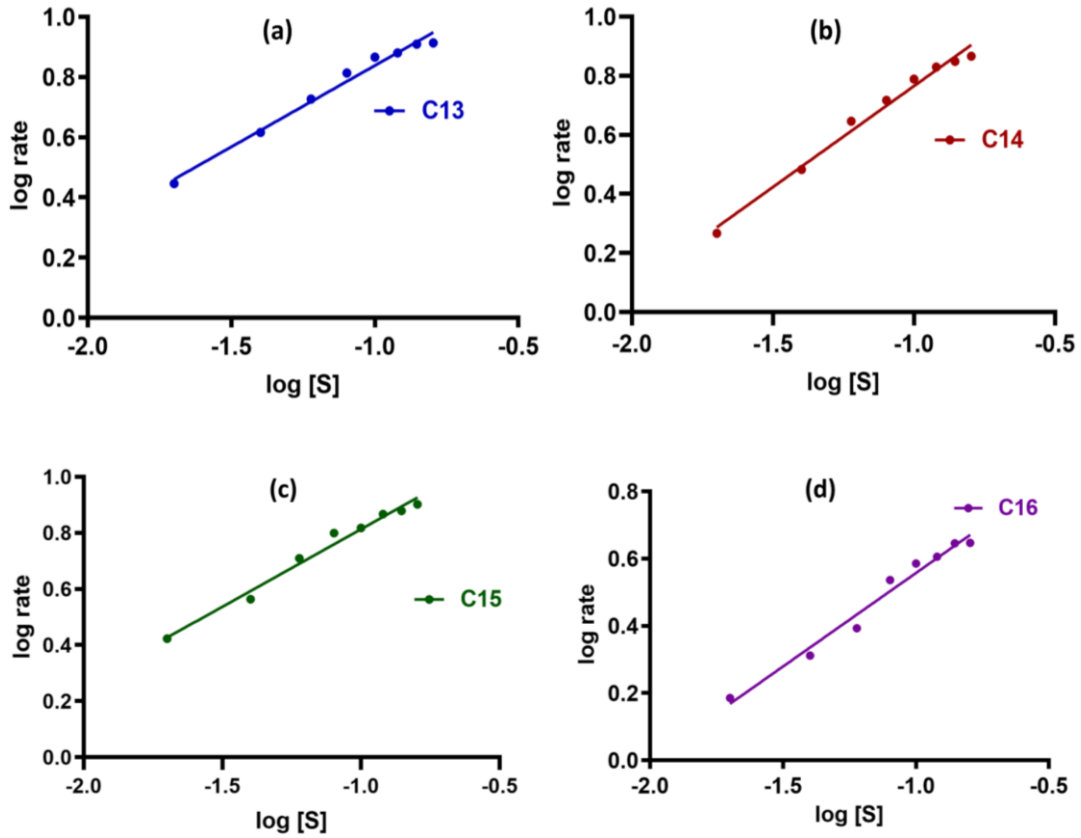

Figure 5.3.4.3 *Plot of log(rate) vs log[S] for complexes (a)* ***C13*** *(b)* ***C14*** *(c)* ***C15*** *(d)* ***C16***

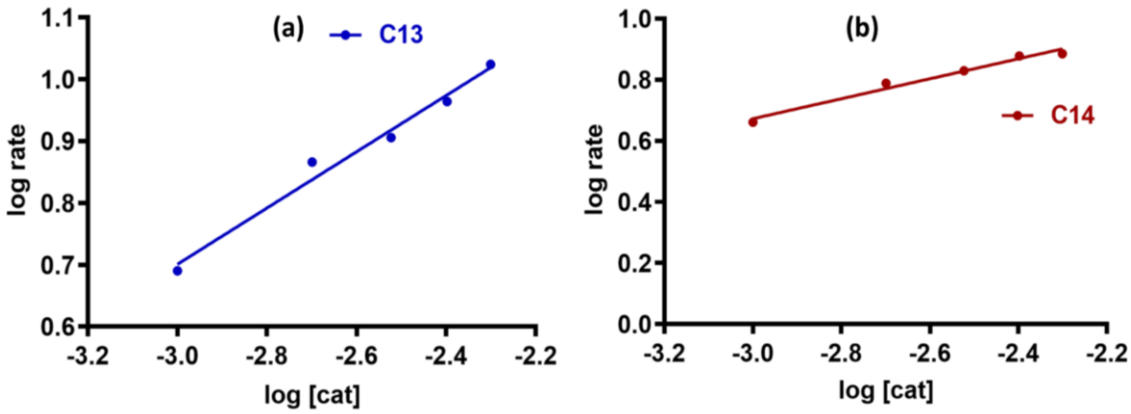

Figure 5.3.4.4 *Plot of log(rate) vs log [Cat] for complexes (a)* ***C13*** *(b)* ***C14***

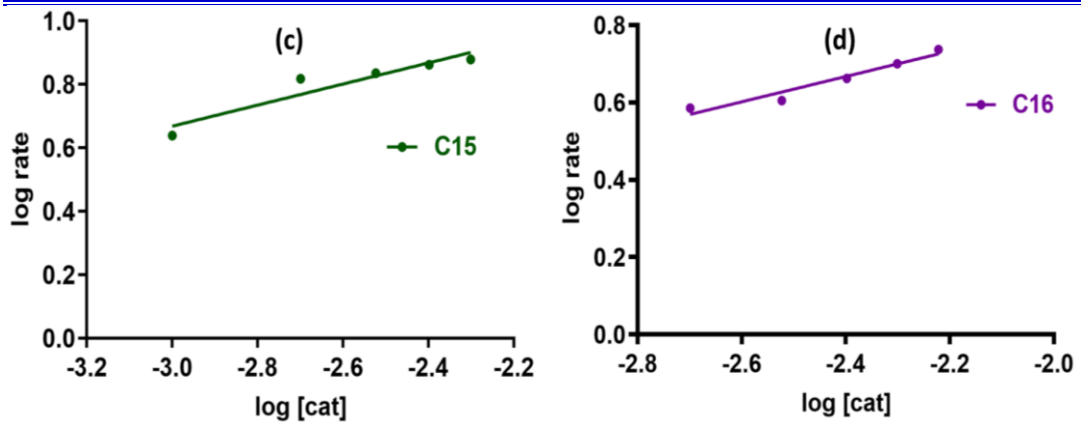

Figure 5.3.4.4 *(Contd…) Plot of log(rate) vs log [Cat] for complexes (c)* ***C15*** *(d)* ***C16***

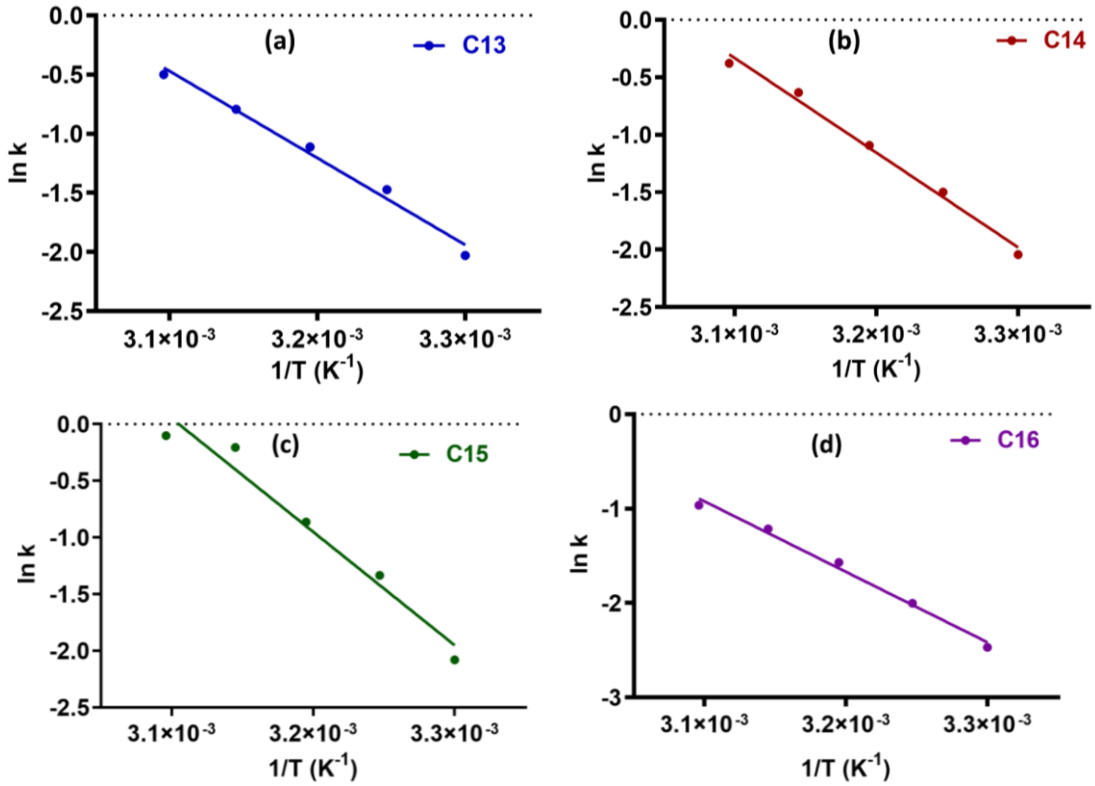

Figure 5.3.4.5 *Arrhenius plot of all complexes (a)* ***C13*** *(b)* ***C14*** *(c)* ***C15*** *and (d)* ***C16***

Activation energy of the reaction was found from the Arrhenius plot (**Figure 5.3.4.5**). The Activation energy required for the conversion of AA to DHAA is in the range of 60-70 kJ/mole.

The kinetic parameters of AA in the presence of complexes, order and activation energy are summarised in **Table 5.3.4.1.**

Table 5.3.4.1 *Kinetic parameters of AA in presence of complexes,* **C13-C16**

Complex	K_m (M)	V_{max} (μM/min)	[E] (M)	k_{cat}/h^{-1}	Order		E_a (kJ/mole)
					Cat	Sub	
C13	12.22	7.27×10^{-5}	2×10^{-6}	367	0.455	0.540	60.95
C14	12.11	1.05×10^{-4}	2×10^{-6}	363	0.327	0.683	68.36
C15	12.0	7.95×10^{-5}	2×10^{-6}	360	0.333	0.553	63.12
C16	7.24	9.5×10^{-5}	2×10^{-6}	217	0.328	0.557	61.96
AAO[24]	0.08 (mM)	6.5 (10^4 mM/s)		9.7×10^4	-	-	-
Copper Salt	-	-	-	-	-	-	89.085
No complex	-	-	-	-	-	-	138.99

The presence of any superoxide formed during the reaction was checked spectroscopically and it was found to be absent. (**Figure 2.3.4.6**). The mechanistic pathways of ascorbic acid oxidation involve production of water or hydrogen peroxide. The formation of hydrogen peroxide was confirmed spectrophotometrically using a literature procedure (See SI†: **Fig. S5.24**) as explained in Chapter 2 **section 2.3.4**.[25–27] Based on these observations, it can be said that the same mechanism as suggested earlier in **section 2.3.4** of chapter 2, is operative here.

These results confirm that the complexes possess good ascorbic acid oxidase mimetic activity. The observed kinetic parameters suggest that these complexes have better ascorbic acid oxidase mimetic activity as compared to the other complexes reported in literature[24,28,29]. The activation energy and other kinetic parameters have more or less similar values for all four complexes. This observation is also consistent with the ionization potential and the energy of HOMO theoretically calculated for the DFT optimized geometry of the complexes.

5.3.5 Catecholase activity

Unlike the studies reported so far on the synthetic tyrosinase and catecholase models, which typically employ 3,5-DTBC because of its low reduction potential[30–34] , in the

present study, five substrates, 3,5-DTBC, 4-methyl catechol, dopamine, pyrocatechol and 2,3-dihydroxy naphthalene have employed to study the catecholase activity of all copper(II) complexes. This is with the intention of studying the selectivity of the model compounds towards the substrates. The reaction with dopamine, pyrocatechol and 2,3-dihydroxy naphthalene was found to be very slow and not measurable. The corresponding quinone band in dopamine, pyrocatechol and 2,3-dihydroxy naphthalene had negligible appearance even after 24 hrs of reaction time indicating negligible catalytic activity of the complex for these three substrates. Complex **C13** was found to be active for the oxidation of 3,5-DTBC and 4-methyl catechol as substrates whereas complex **C14-C15** were found to be active with 3,5-DTBC as substrates but complex **C16** was found to be less active for both substrates. Hence, detailed kinetic studies have been carried out with 3,5-DTBC and 4-methyl catechol as substrate for the complexes which were active for these substrates following similar procedures as explained in **section 2.3.5** in Chapter 2.

The substrate 3,5-DTBC or 4-methyl catechol was added at once to the solution of the complex and the spectra were recorded. A new band corresponding to 3,5-DTBQ started appearing at 380–410 nm along with LMCT band. A linear increase in the absorption of this band was observed. The course of a typical reaction with solution of complex **C13** is presented in **Figure 5.3.5.1 (a**) for 3,5-DTBC as substrate. Those for other complexes and substrates are presented in SI† in **Fig 5.21(a)** and **5.22-5.23 (a)** inset graph. The kinetics of oxidation of 3,5-DTBC was determined by the method of initial rates as a function of time (**figure 5.3.5.1 (b-d)** for **C13** (3,5-DTBC) and SI† **Fig. 5.21-5.23(b-d)** for other complexes for same substrate).

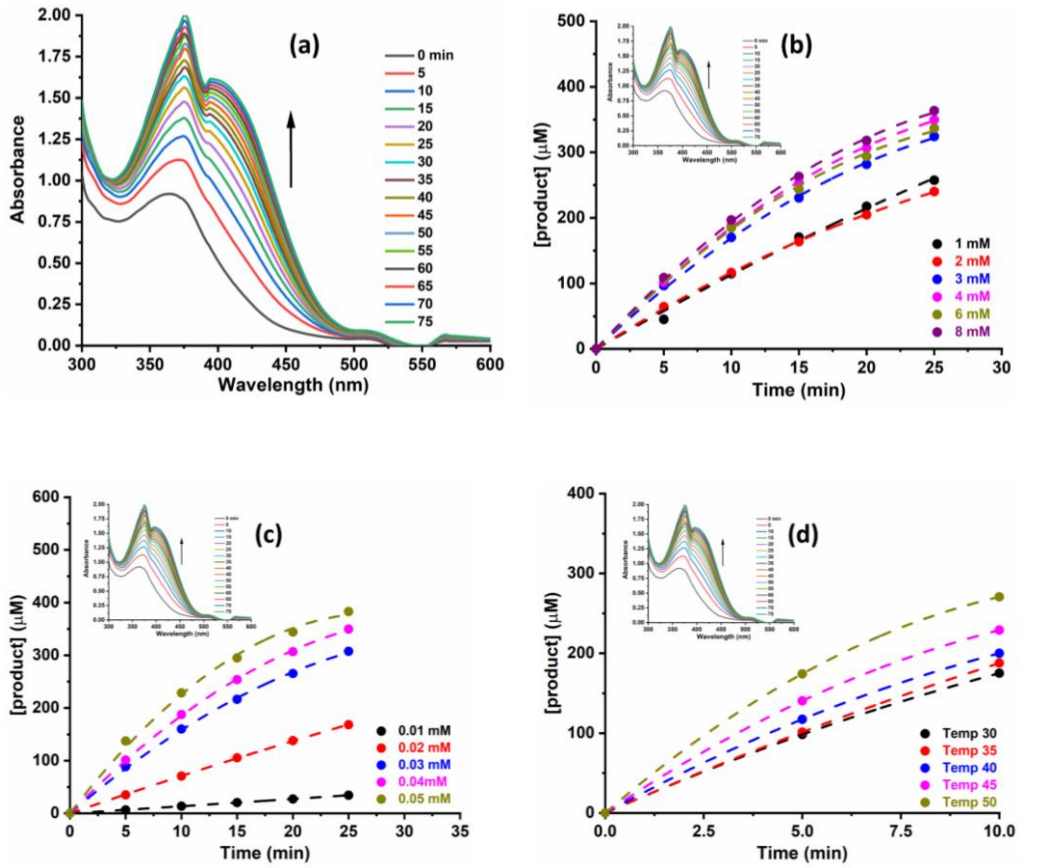

Figure 5.3.5.1 *(a) Time dependent spectral changes over a time period of 3,5-DTBC corresponding to* ***C13*** *catalyzed oxidation and (b-d) Plot of [product] as function of time with respect to substrate (b), catalyst (c) and temperature (d) (Inset: Plot of absorbance vs wavelength at different time interval) for complex* ***C13*** *with 3,5-DTBC*

The analysis of the data based on the Michaelis- Menten model, originally developed for enzyme kinetics, was applied. In **figure 5.3.5.2 (a-d)**, the solid circles are experimental data and the solid curves are the fits to the Michaelis-Menten model for all complexes with 3,5-DTBC. With various concentrations of substrates, Michaelis-Menten constant (K_m) and V_{max} values can be obtained from the Michaelis Menten equation. The Lineweaver-Burk plot for all complexes with 3,5-DTBC and complex **C13** with 4-MC are depicted in inset of **Figure 5.3.5.2 (a-d)**. The k_{cat} values of the respective complexes of particular substrates were calculated and are listed in **Table 5.3.5.1.**

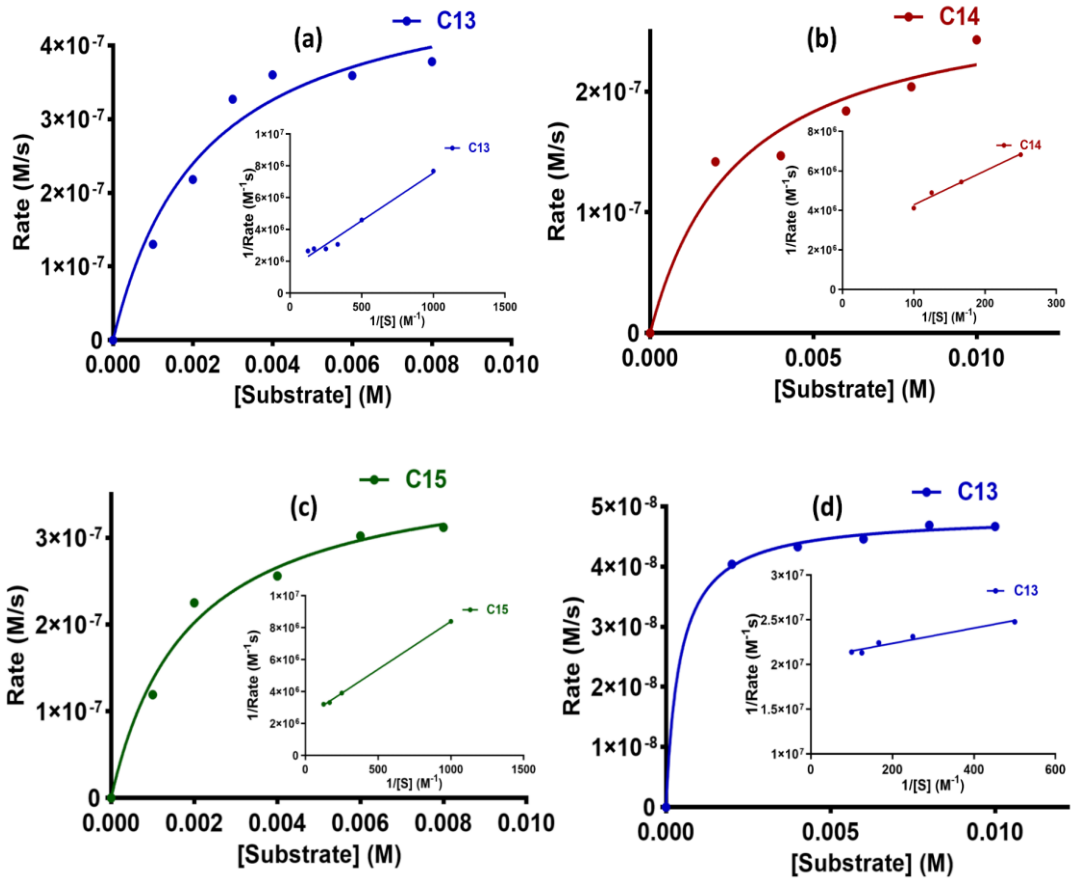

Figure 5.3.5.2 *Plot of Rate vs [Substrate]of Michaelis Menten model for complexes (a)* ***C13*** *(b)* ***C14*** *(c)* ***C15*** *for 3,5-DTBC and (d)* ***C13*** *for 4-MC (Inset: Lineweaver Burk plot)*

The plots of log (rate) versus log[substrate] (**Figure 5.3.5.3 (a-d)**) and log (rate) versus log[catalyst] (**figure 5.3.5.4 (a-d)**) for 3,5-DTBC of all complexes indicate that the complex catalysed oxidation of 3,5-DTBC to the corresponding quinones follow first order kinetics with respect to the substrate and also with respect to the dicopper(II) complexes.

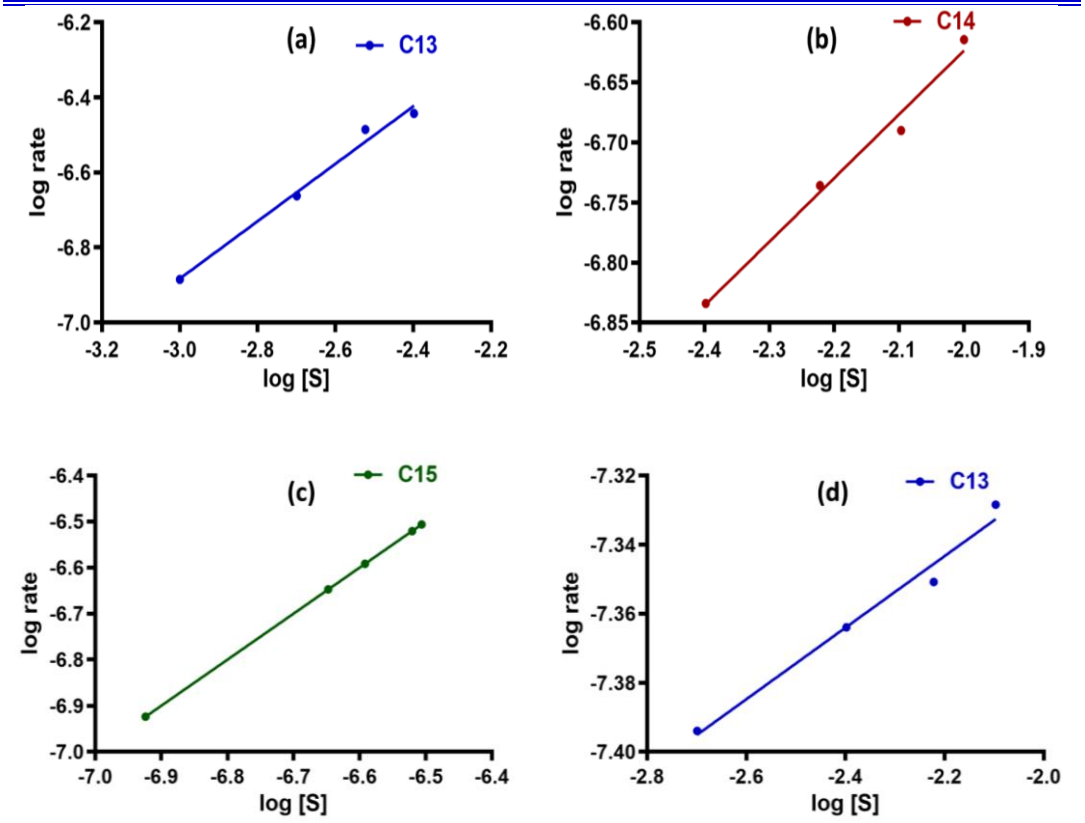

Figure 5.3.5.3 *Plot of log rate vs log [Sub] for complexes (a)* ***C13*** *(b)* ***C14*** *(c)* ***C15*** *for 3,5-DTBC and (d)* ***C13*** *for 4-MC*

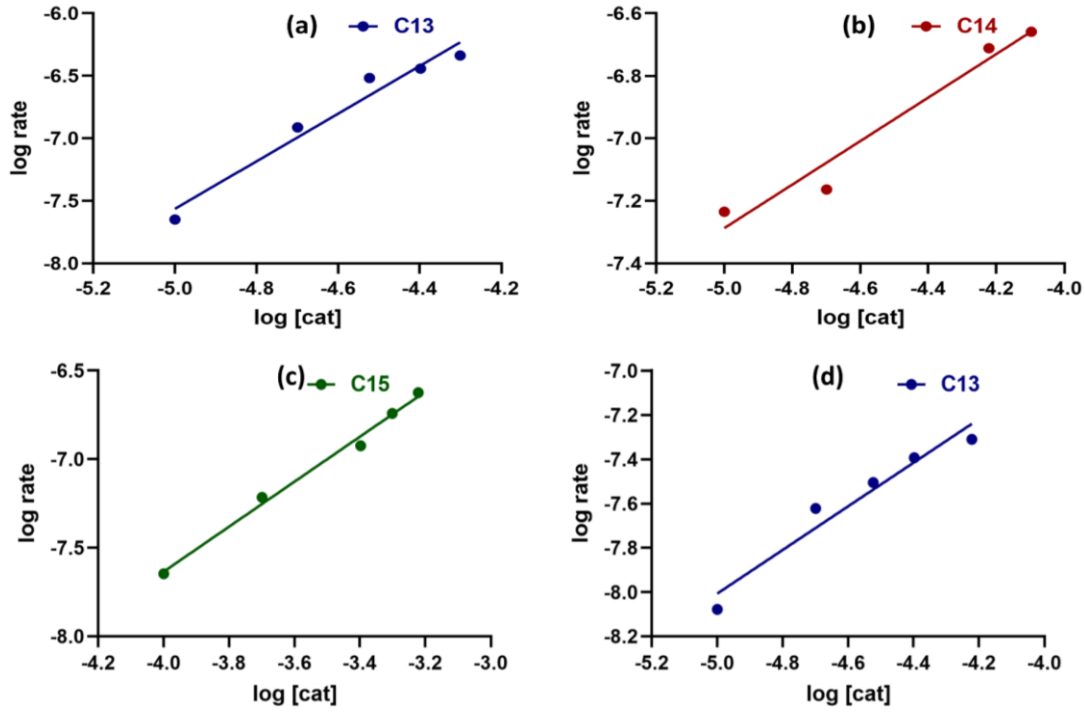

Figure 5.3.5.4 *Plot of log rate vs log [Cat] for complexes (a)* ***C13*** *(b)* ***C14*** *(c)* ***C15*** *for 3,5-DTBC and (d)* ***C13*** *for 4-MC*

The activation energy values for the oxidation of 3,5-DTBC was found to be in the range of 12.9-16.39 kJ/mole in presence of all synthesized complexes **(C13-C15**) as catalyst and that of 4-methyl catechol was found to be 41.99kJ/mole in presence of complex **C13** as calculated from Arrhenius plots (**figure 5.3.5.5 (a-d)**).

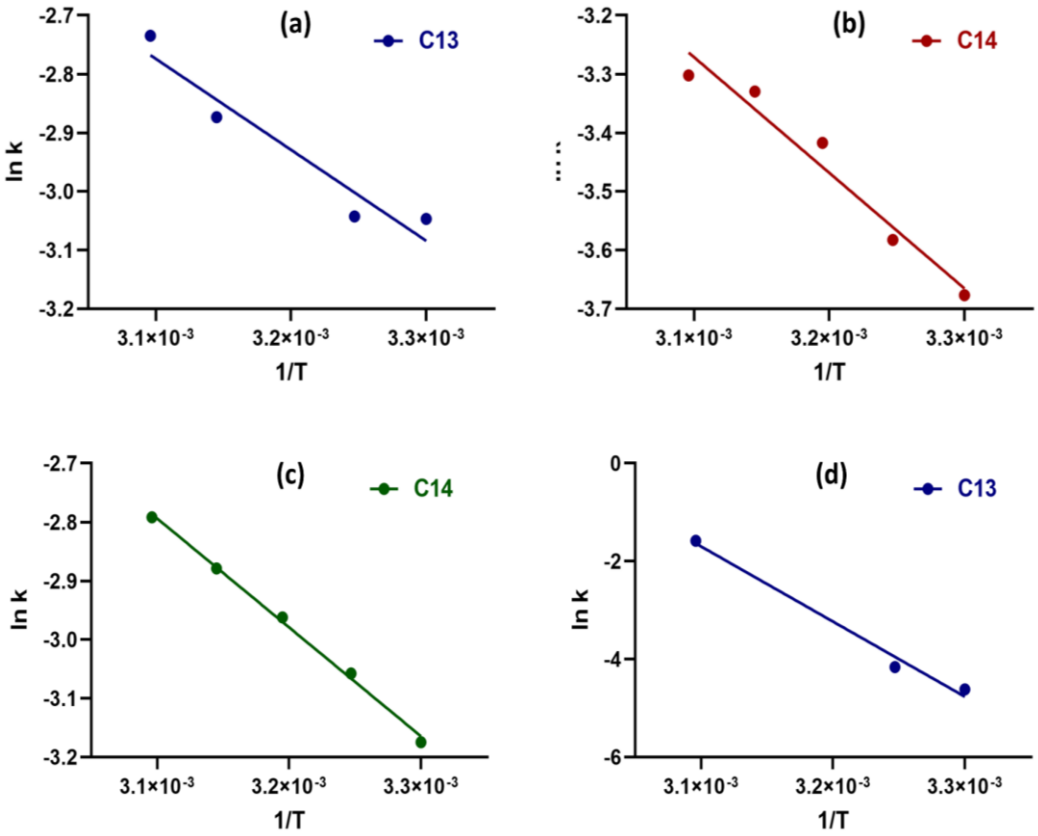

Figure 5.3.5.5 *Arrhenius plot of all complexes (a)* ***C13*** *(b)* ***C14*** *(c)* ***C15*** *for 3,5-DTBC and (d)* ***C13*** *for 4-MC*

The kinetic parameters with both substrates of all synthesized complexes, order with respect to catalyst as well as substrate and activation energy are listed in **Table 5.3.5.1**. The activation energy for the complex catalysed oxidation of 3,5-DTBC follows the order **C13 > C15 > C14**. This is similar to the order of energy of HOMO and the ionization potentials calculated for the optimized geometry of the respective complexes.

Table 5.3.5.1 *Kinetic parameters of Michaelis Menten model, Order, Activation energy of 3,5-DTBC with different complexes*

Complexes	Substrates	V_{max} (M/s)	K_m (M)	k_{cat} (h^{-1})	Order		E_a (kJ/mole)
					Cat	Sub	
C13	3,5-DTBC	5.11×10^{-7}	2.27×10^{-2}	45.99	1.905	0.7649	12.90
	4-MC	4.85×10^{-8}	4.23×10^{-4}	4.365	0.986	0.966	41.99
C14	3,5-DTBC	2.82×10^{-7}	2.71×10^{-3}	25.38	0.696	0.530	16.39
C15	3,5-DTBC	3.89×10^{-7}	1.85×10^{-3}	35.01	1.270	1.00	15.41

The presence of any superoxide formed during the reaction was checked spectroscopically and it was found to be absent. (**Figure 2.3.5.6**). The mechanistic pathways of catechol oxidation involve production of water or hydrogen peroxide. The formation of hydrogen peroxide was confirmed spectrophotometrically using a literature procedure (See SI†: **Fig. S5.24**) as explained in Chapter 2 **section 2.3.5**.[25–27] Based on these observations, it can be said that the same mechanism as suggested earlier in **section 2.3.5** of chapter 2, is operative here.

5.4 CONCLUSION

- Synthesis and characterisation of four new binucleating ligands (**L^{13}-L^{16}**) and its dicopper(II) complexes (**C13-C16**) has been carried out.
- Kinetics of Ascorbic acid oxidase activity and catecholase activity of dicopper(II) complexes with ascorbic acid and 3,5-DTBC & 4-methyl catechol as substrates has been studied by varying parameters like concentration of substrate and catalyst and temperature.
- SOD mimic activity of dicopper complexes has been studied.
- Complex **C13** has significantly high SOD mimic activity over other complexes in the following order: **C13 > C15 > C14 > C16**.
- Complexes **C13-16** have somewhat similar ascorbic acid oxidase activity.
- **Complex C13** have better catecholase activity as compared to other complexes with 3,5-DTBC and **C13** is only active for 4-methyl catechol

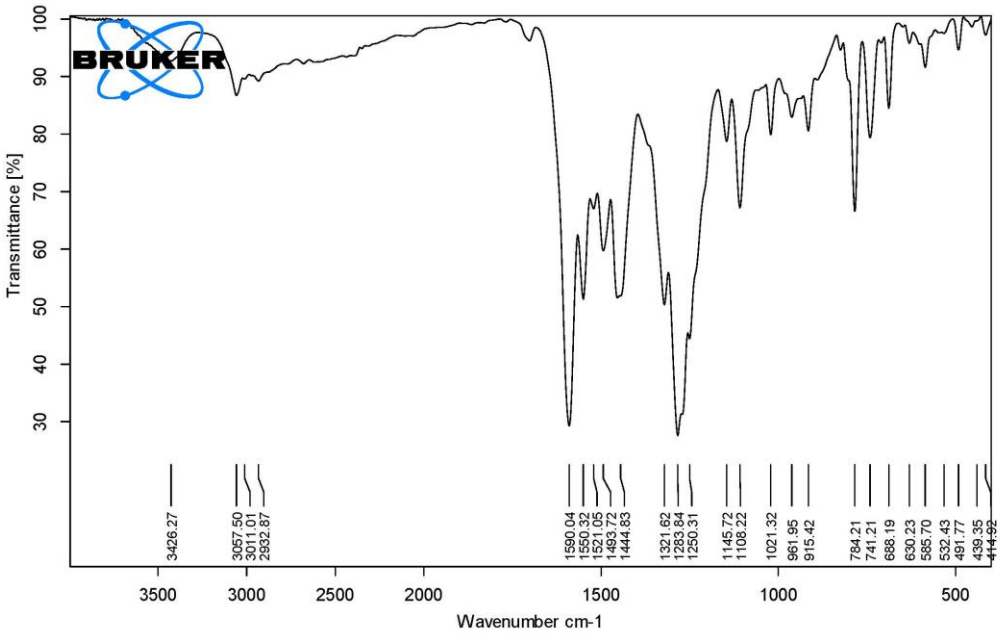

Fig. S5.1 *IR spectrum of* ***L[13]***

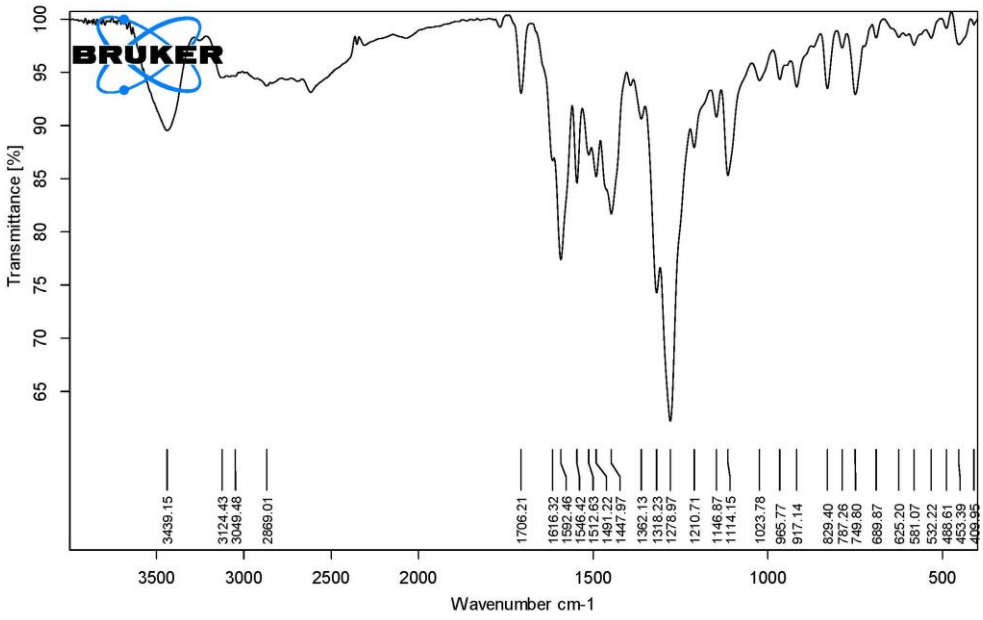

Fig. S5.2 *IR spectrum of* ***L[14]***

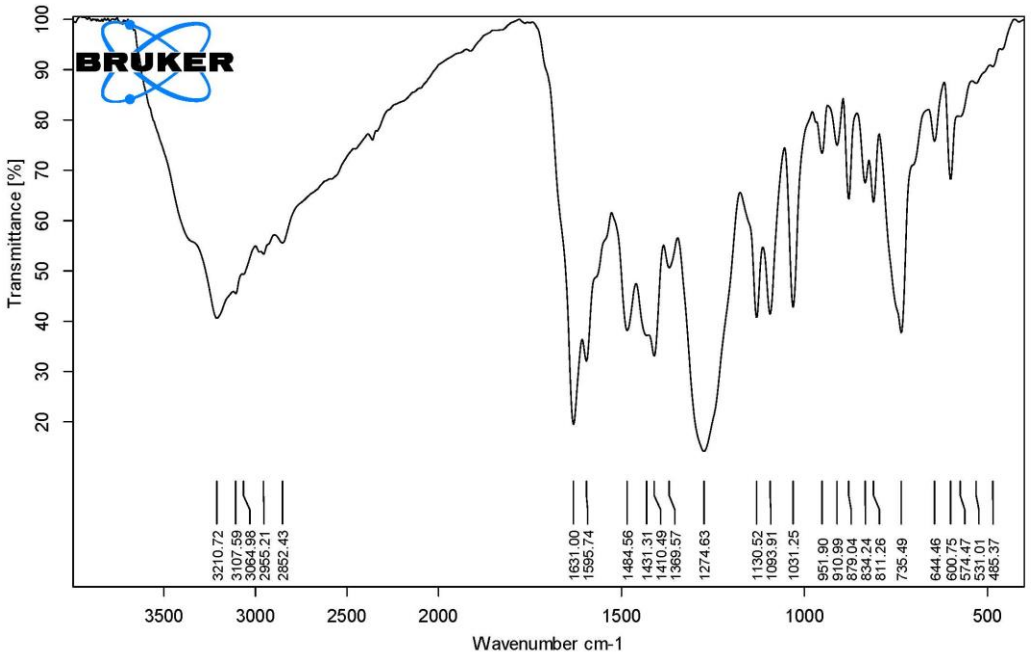

Fig. S5.3 *IR spectrum of* ***L[15]***

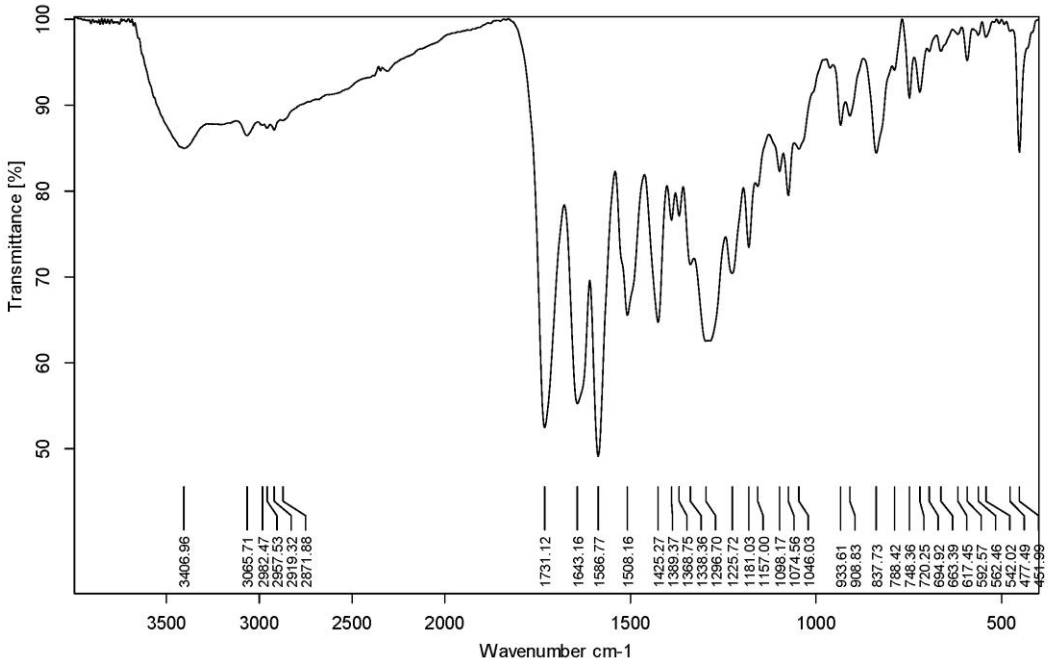

Fig. S5.4 *IR spectrum of* ***L[16]***

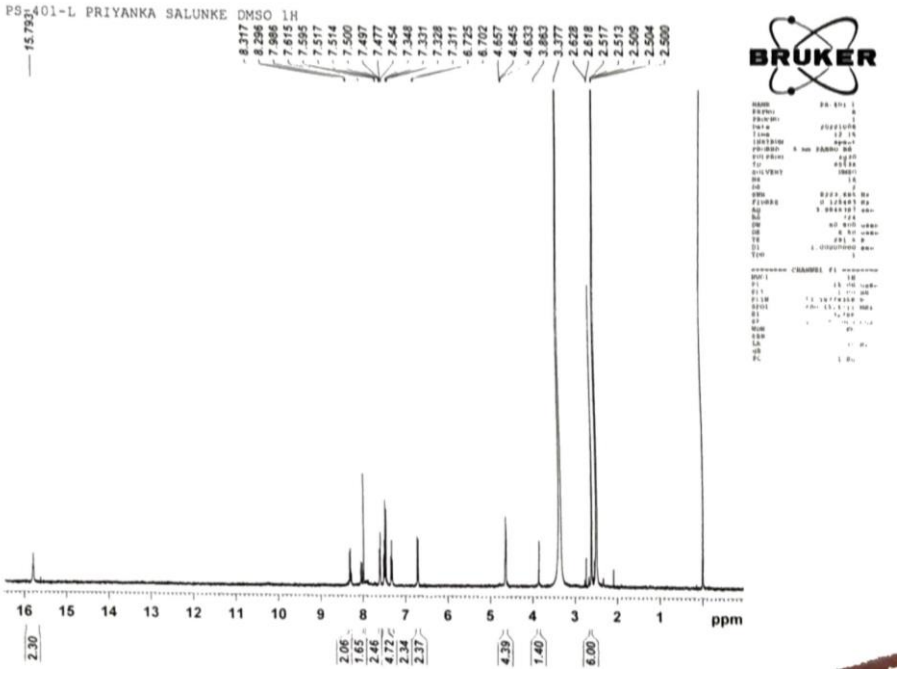

Fig. S5.5 *[1]NMR spectrum of* ***L[13]***

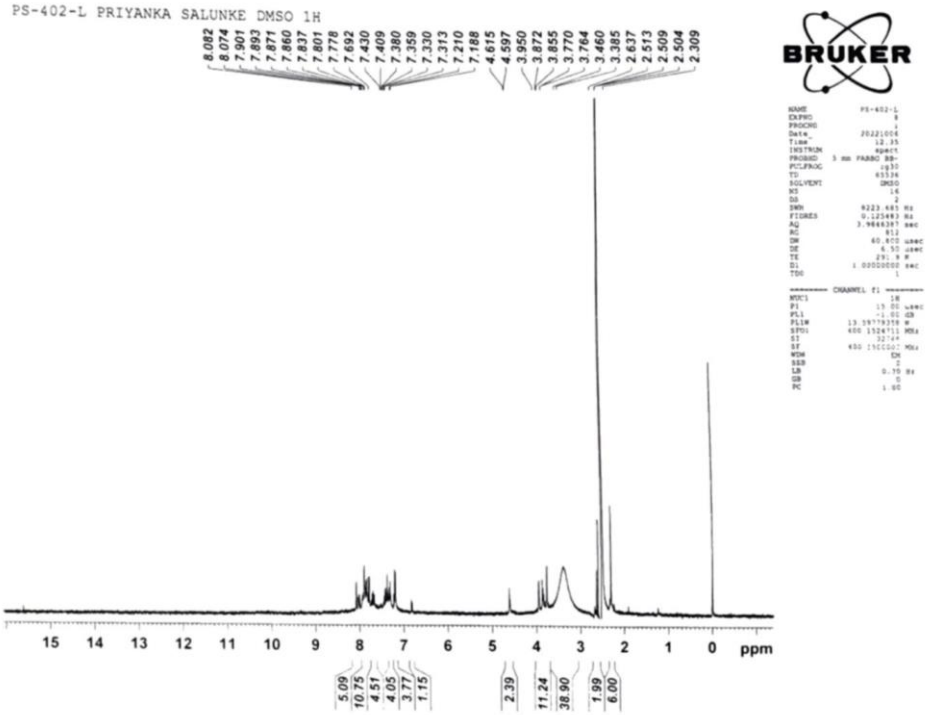

Fig. S5.6 *[1]NMR spectrum of* ***L[14]***

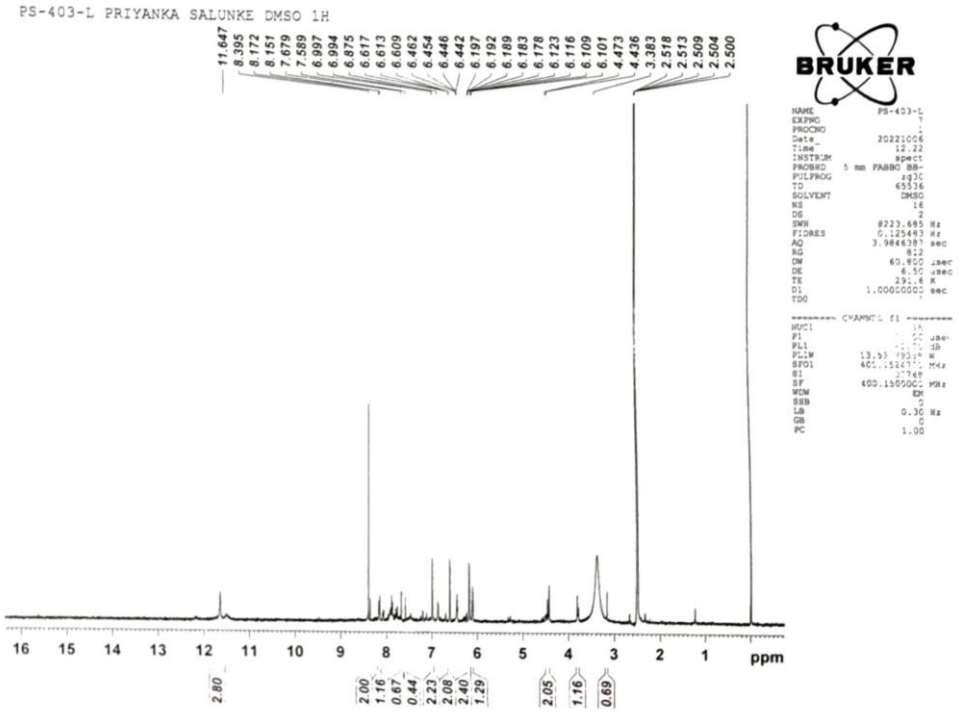

Fig. S5.7 *^{1}NMR spectrum of* ***L^{15}***

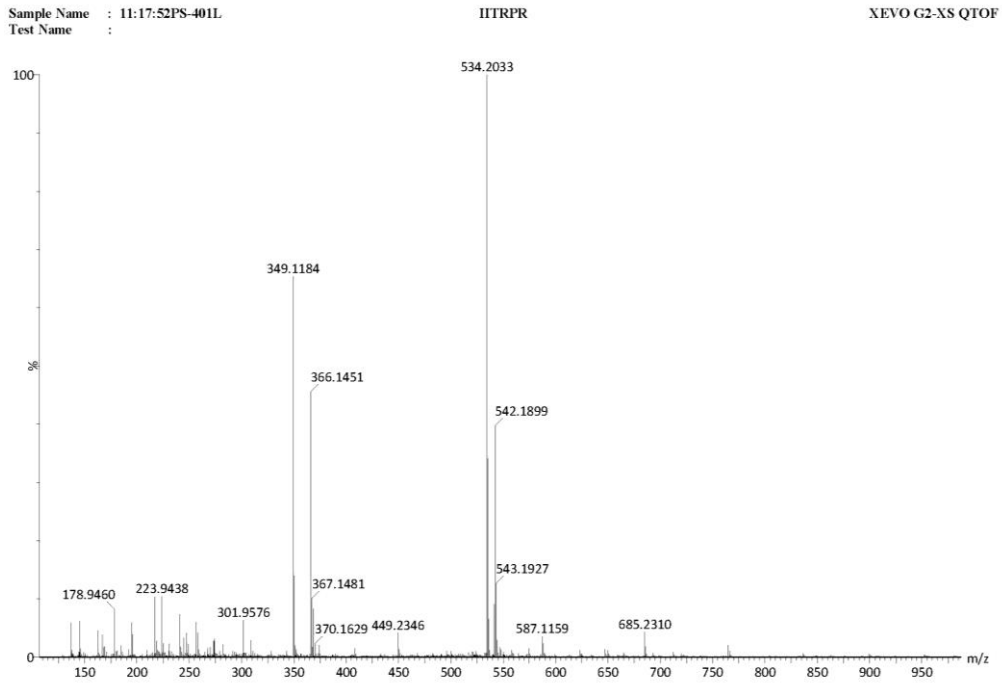

Fig. S5.8 *Mass spectrum of* ***L[13]***

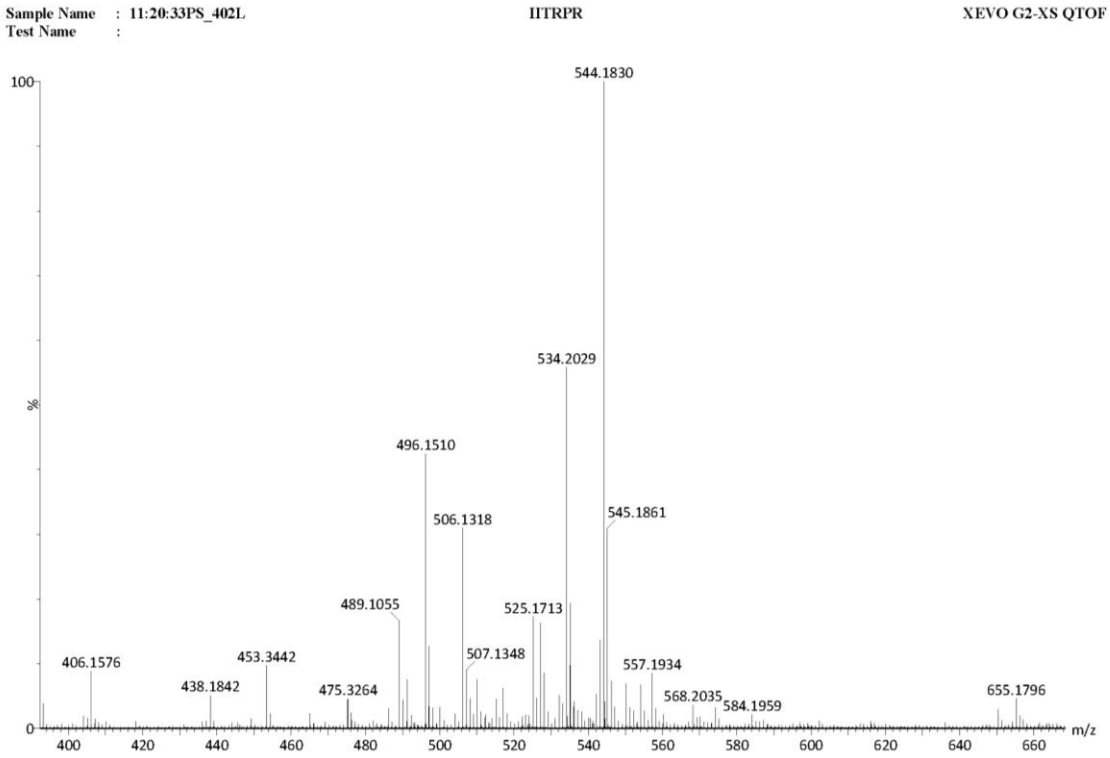

Fig. S5.9 *Mass spectrum of* ***L[14]***

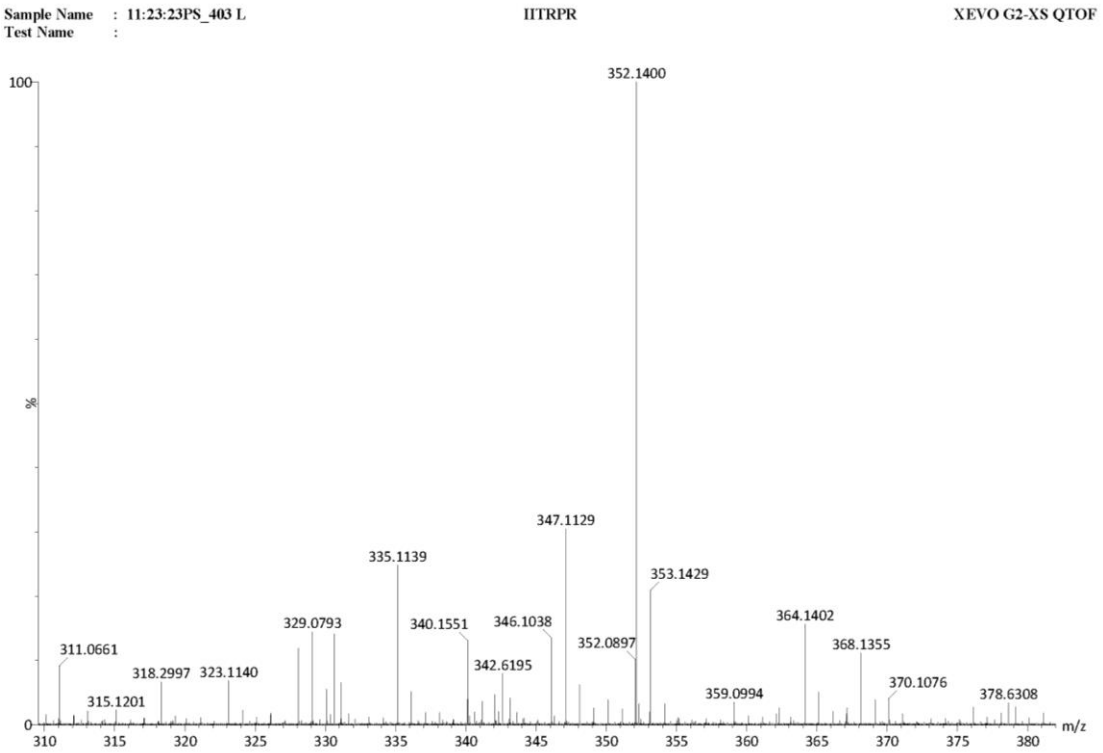

Fig. S5.10 *Mass spectrum of* ***L[15]***

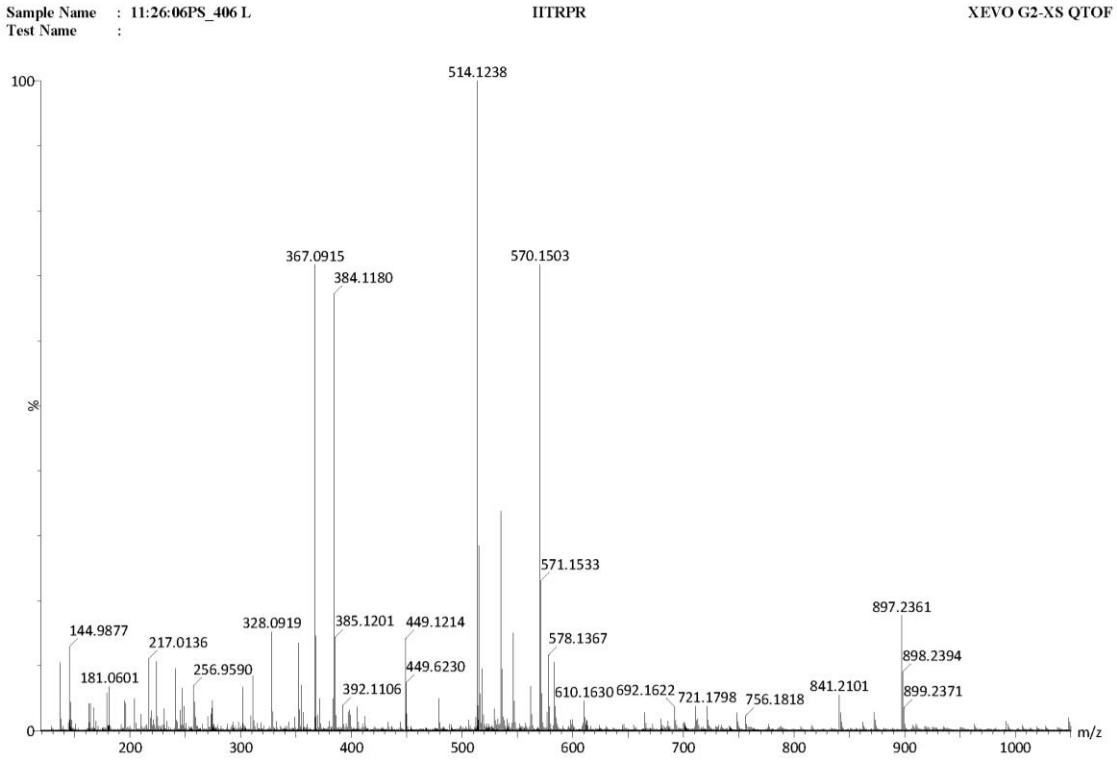

Fig. S5.11 *Mass spectrum of* ***L[16]***

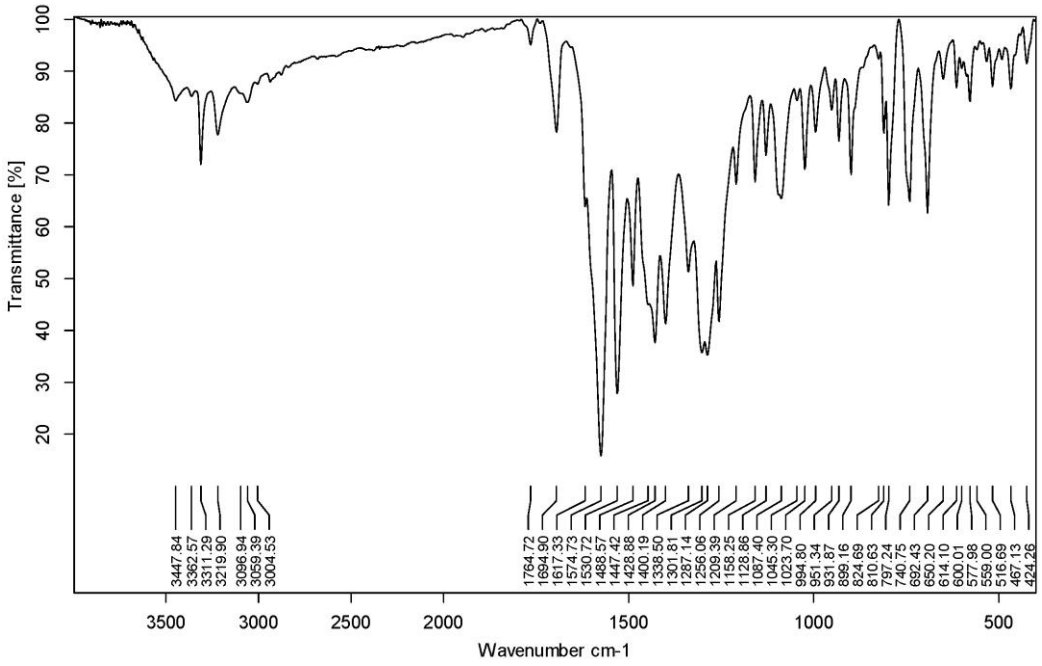

Fig. S5.12 *IR spectrum of* ***C13***

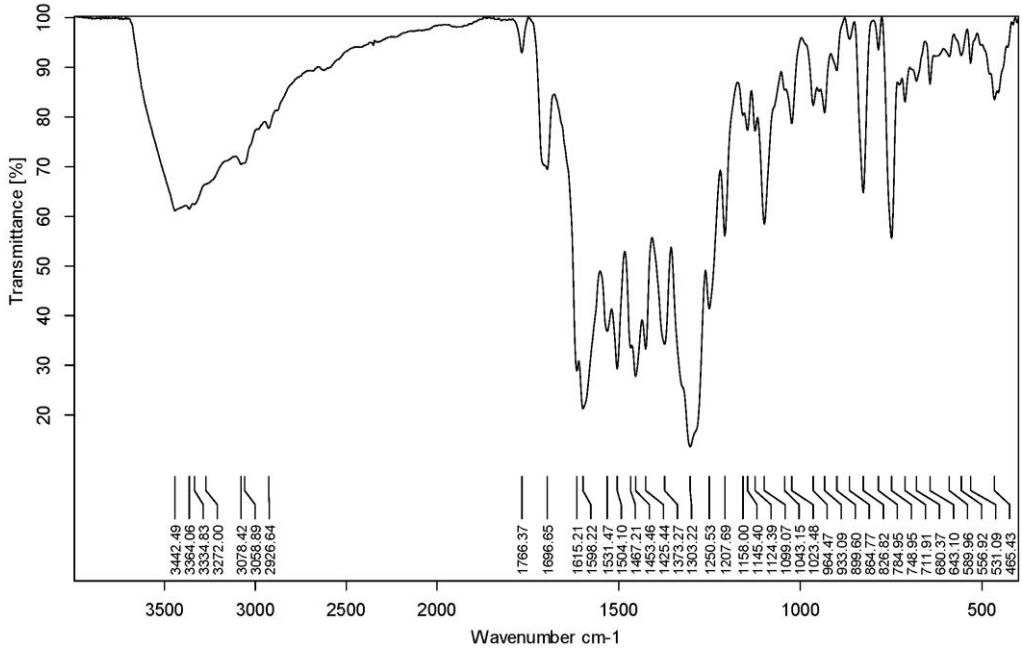

Fig. S5.13 *IR spectrum of* ***C14***

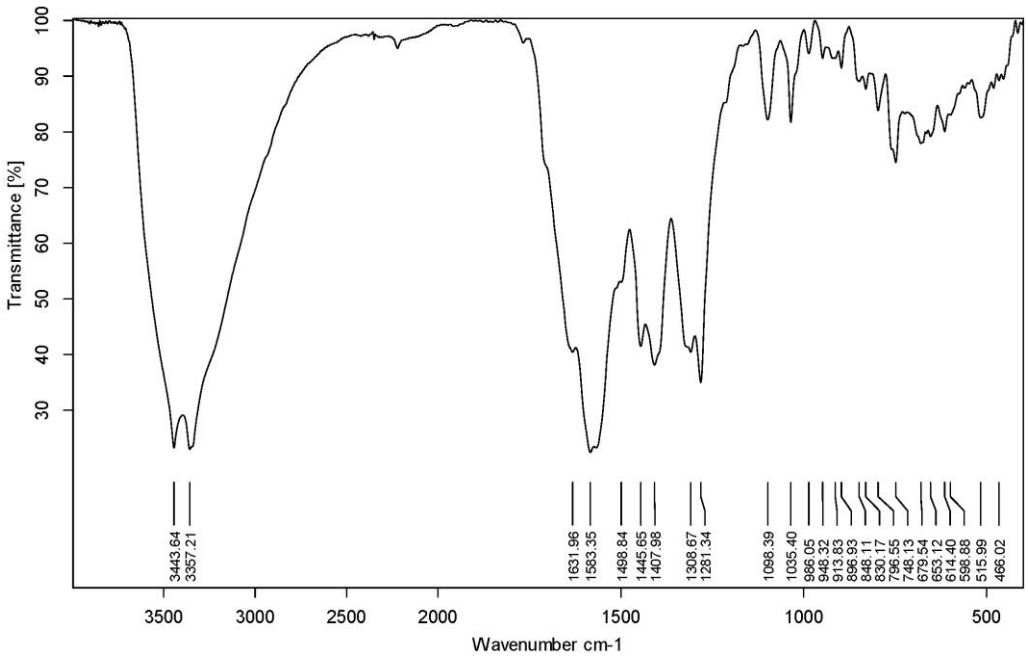

Fig. S5.14 *IR spectrum of* ***C15***

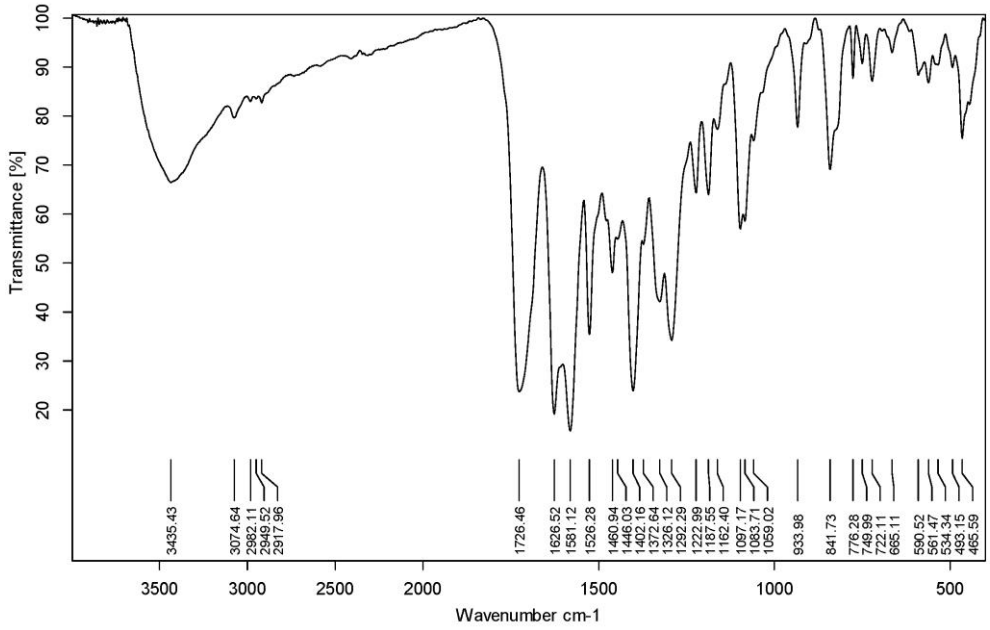

Fig. S5.15 *IR spectrum of* ***C16***

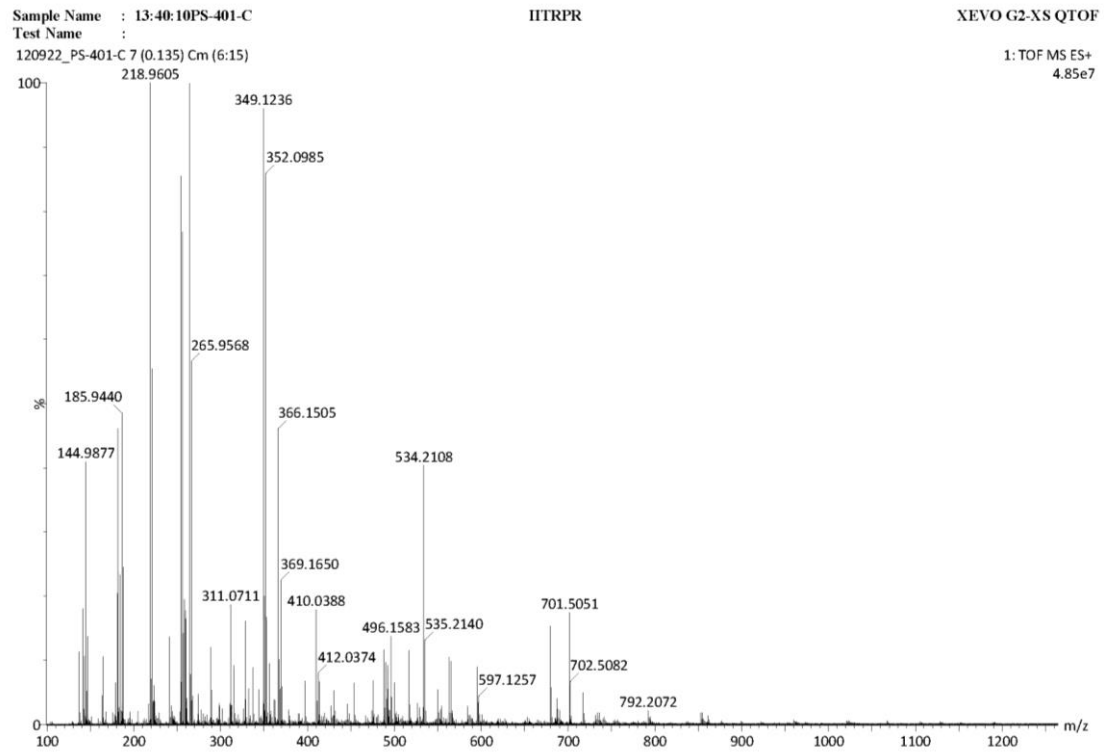

Fig. S5.16 *Mass spectrum of* ***C13***

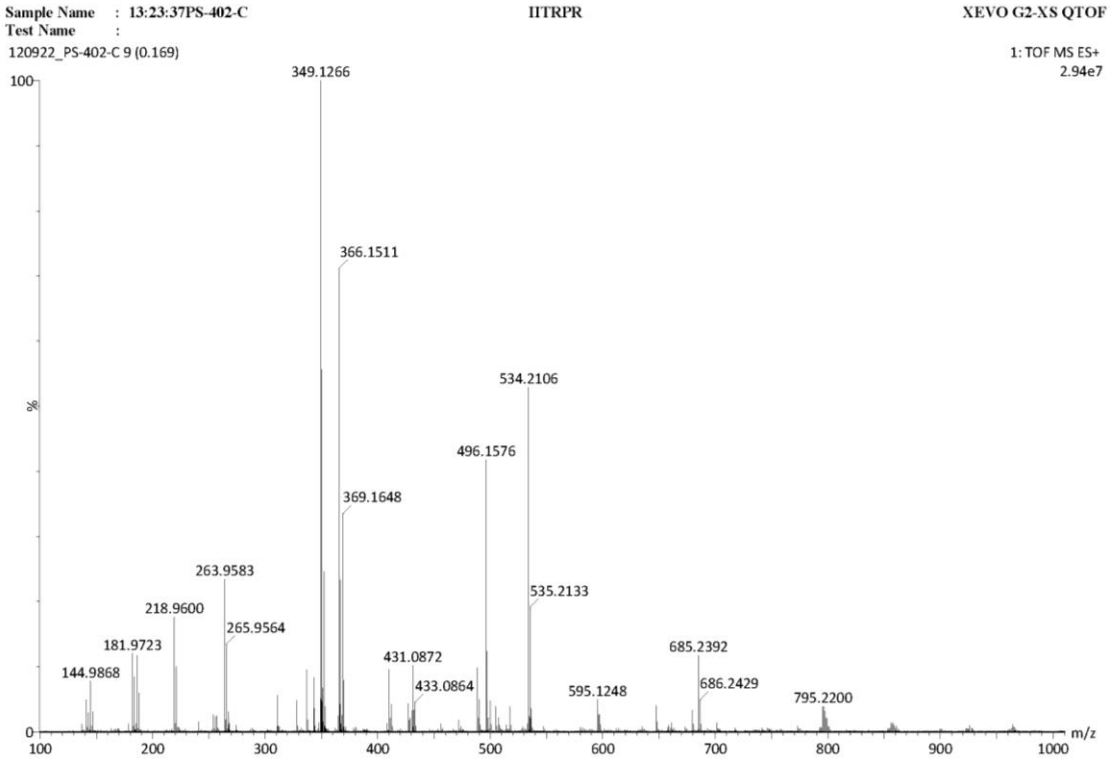

Fig. S5.17 *Mass spectrum of* ***C14***

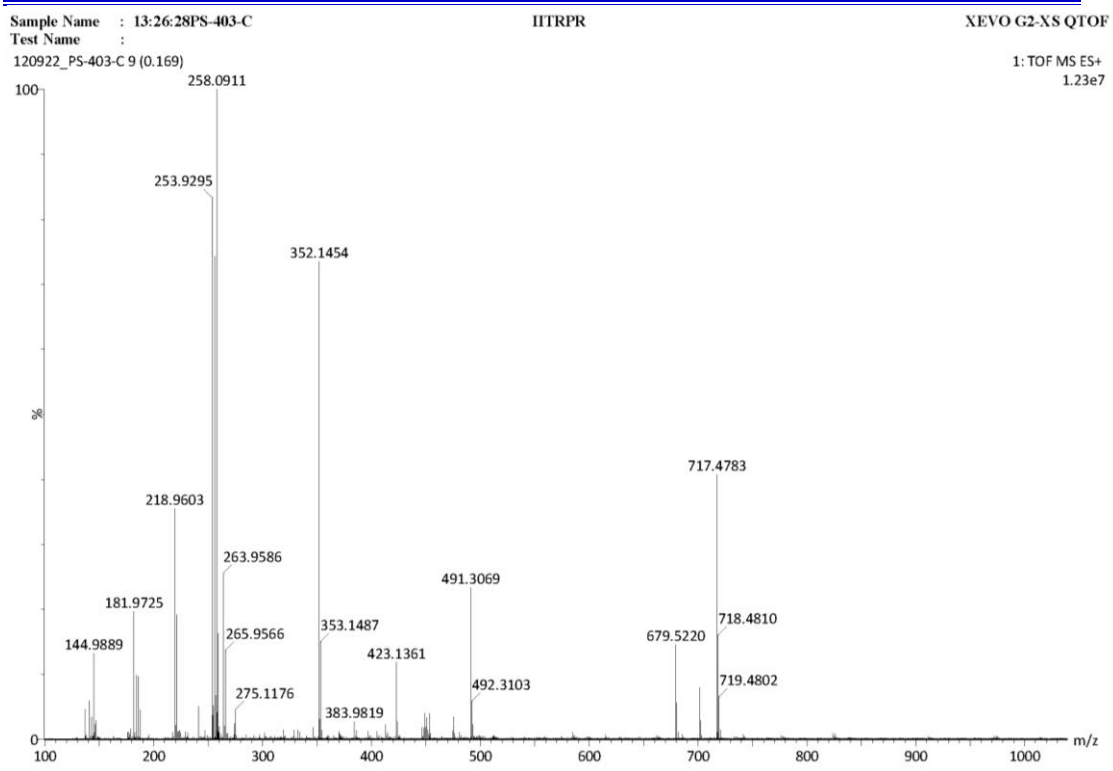

Fig. S5.18 *Mass spectrum of* ***C15***

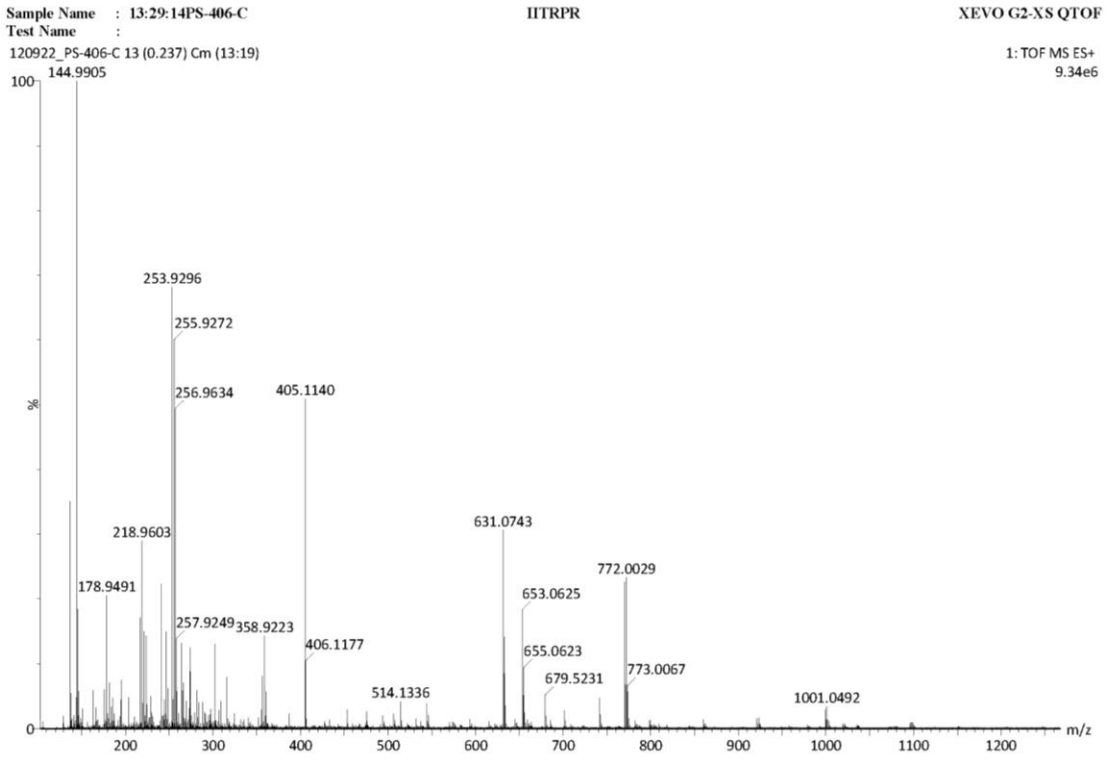

Fig. S5.19 *Mass spectrum of* ***C16***

Table S5.1 *Bond lengths and Bond angles of complexes,* ***C13-C14***

C13		
Cu-N Distances (Aº)		
R(19,72)	N19-Cu72	1.9759
R(18,73)	N18-Cu73	1.9765
Cu-O Distances (Aº)		
R(30,72)	O30-Cu72	2.042
R(30,73)	O30-Cu73	2.0412
R(64,72)	O64-Cu72	1.9655
R(63,73)	O63-Cu73	1.9651
R(70,72)	O70-Cu72	1.9662
R(71,73)	O71-Cu73	1.9671
Bond angles		
A(19,72,30)	N19-Cu72-O30	95.3378
A(19,72,64)	N19-Cu72-O64	90.8866
A(30,72,70)	O30-Cu72-O70	98.6287
A(64,72,70)	O64-Cu72-O70	94.4713
A(18,73,30)	N18-Cu73-O30	95.3478
A(18,73,63)	N18-Cu73-O63	90.8842
A(30,73,71)	O30-Cu73-O71	98.5517
A(63,73,71)	O63-Cu73-O71	94.458
C14		
Cu-N Distances (Aº)		
R(19,45)	N19-Cu45	1.9685
R(18,46)	N18-Cu46	1.9767
Zn-O Distances (Aº)		
R(30,45)	O30-Cu45	2.0569
R(30,46)	O30-Cu46	2.0015
R(44,45)	O44-Cu45	1.9878
R(43,46)	O43-Cu46	1.9716
R(64,45)	O64-Cu45	1.9638
R(69,46)	O69-Cu46	1.9477
Bond angles		
A(19,45,30)	N19-Cu45-O30	95.084
A(19,45,44)	N19-Cu45-O44	90.4401
A(30,45,64)	O30-Cu45-O64	100.2664
A(44,45,64)	O44-Cu45-O64	107.6296
A(18,46,30)	N18-Cu46-O30	94.3652
A(18,46,43)	N18-Cu46-O43	86.4217
A(30,46,69)	O30-Cu46-O69	92.8837
A(43,46,69)	O43-Cu46-O69	90.485

Table S5.1 (*Contd..****)*** *Bond lengths and Bond angles of complex* ***C15***

C15		
Cu-N Distances (Aº)		
R(5,82)	N5-Cu82	**2.0055**
R(31,83)	N31-Cu83	**2.0435**
R(80,82)	N80-Cu82	**2.0417**
Cu-O Distances (Aº)		
R(6,83)	O6-Cu83	**2.0055**
R(6,82)	O6-Cu82	**2.0503**
R(81,82)	O81-Cu82	**2.0542**
R(81,83)	O81-Cu83	**2.1594**
R(97,82)	O97-Cu82	**2.2222**
R(100,83)	O100-Cu83	**2.032**
Bond angles		
A(5,82,6)	N5-Cu82-O6	**84.9472**
A(5,82,80)	N5-Cu82-N80	**104.7981**
A(5,82,97)	N5-Cu82-O97	**92.8123**
A(6,82,81)	O6-Cu82-O8	**77.1744**
A(6,82,97)	O6-Cu82-O97	**114.2942**
A(80,82,81)	N80-Cu82-O81	**86.077**
A(80,82,97)	N80-Cu82-O97	**91.1623**
A(81,82,97)	O81-Cu82-O97	**106.6312**
A(6,83,81)	O6-Cu83-O81	**76.8319**
A(6,83,100)	O6-Cu83-O100	**94.8637**
A(31,83,81)	N31-Cu83-O81	**121.3466**
A(81,83,100)	O81-Cu83-O100	**107.8257**
A(6,83,31)	O6-Cu83-N31	**80.7071**
Torsional angles		
L(98,83,100,6,-1)	O98-Cu83-O100-O6 (-1)	**159.6972**
L(98,83,100,6,-2)	O98-Cu83-O100-O6 (-2)	**168.5995**

Table S5.1 (*Contd..****)*** *Bond lengths and Bond angles of complex* ***C16***

C16		
Cu-N Distances (Aº)		
R(8,63)	N8-Cu63	**1.9523**
R(9,64)	N9-Cu64	**1.953**
Cu-O Distances (Aº)		
R(34,63)	O34-Cu63	**2.0233**
R(34,64)	O34-Cu64	**2.0223**
R(35,64)	O35-Cu64	**1.9694**
R(36,63)	O36-Cu63	**1.9703**
R(70,63)	O70-Cu63	**1.9592**
R(71,64)	O64-Cu64	**1.962**
Bond angles		
A(9,64,35)	N9-Cu64-O35	**92.2438**
A(34,64,71)	O34-Cu64-O71	**96.4503**
A(35,64,71)	O35-Cu64-O71	**91.1954**
A(9,64,34)	N9-Cu64-O34	**93.7209**
A(8,63,34)	N8-Cu63-O34	**93.6999**
A(8,63,36)	N8-Cu63-O36	**92.2157**
A(34,63,70)	O34-Cu63-O70	**92.2157**
A(36,63,70)	O36-Cu63-O70	**91.1788**

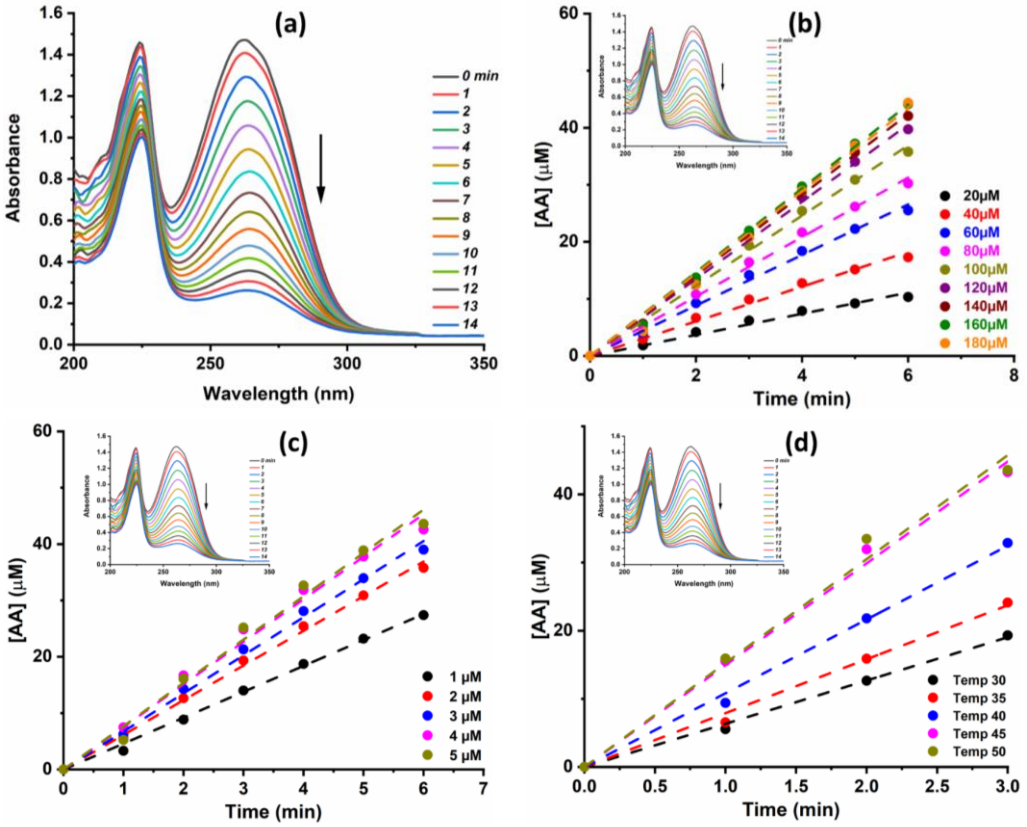

Fig. S5.20A *(a) Time dependent spectral changes from 0 to 14 mins of AA corresponding to* ***C14*** *catalyzed oxidation and (c-e) Plot of [AA] as function of time with respect to substrate (c), catalyst (d) and temperature (e) (Inset: Plot of absorbance vs wavelength at different time interval) with AA*

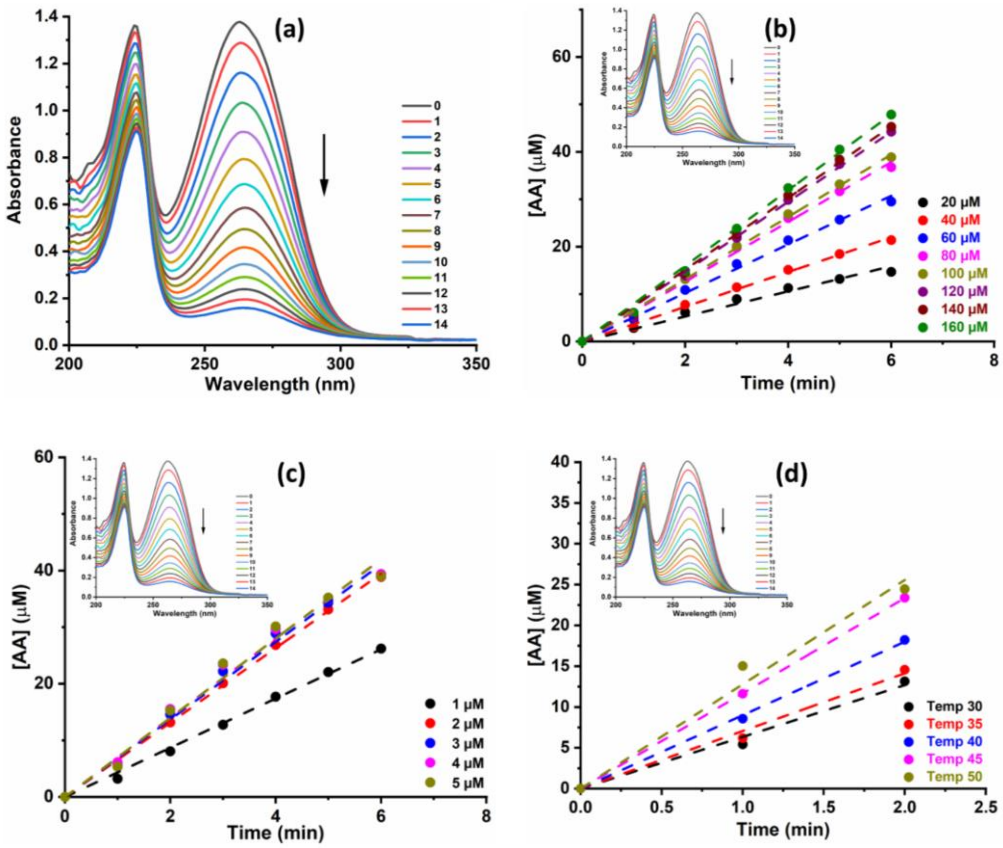

Fig. S5.20B *(a) Time dependent spectral changes from 0 to 14 mins of AA corresponding to* ***C15*** *catalyzed oxidation and (c-e) Plot of [AA] as function of time with respect to substrate (c), catalyst (d) and temperature (e) (Inset: Plot of absorbance vs wavelength at different time interval) with AA*

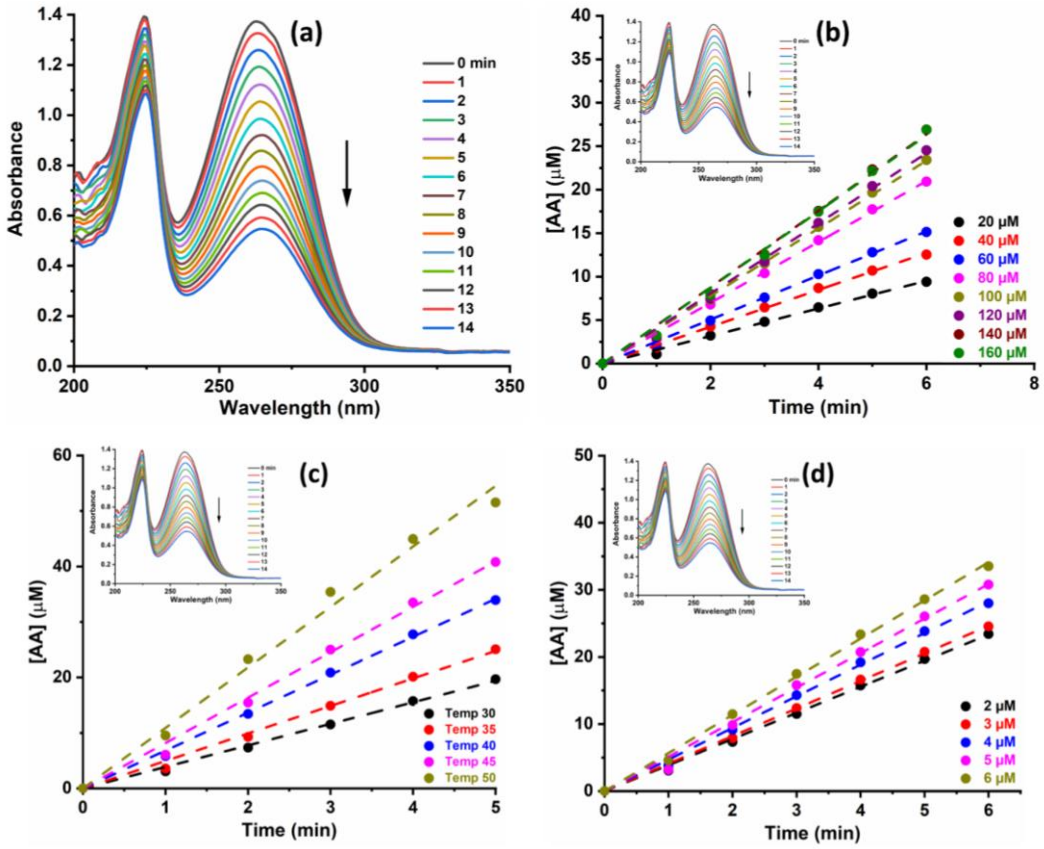

Fig. S5.20C *(a) Time dependent spectral changes from 0 to 14 mins of AA corresponding to* ***C16*** *catalyzed oxidation and (c-e) Plot of [AA] as function of time with respect to substrate (c), catalyst (d) and temperature (e) (Inset: Plot of absorbance vs wavelength at different time interval) with AA*

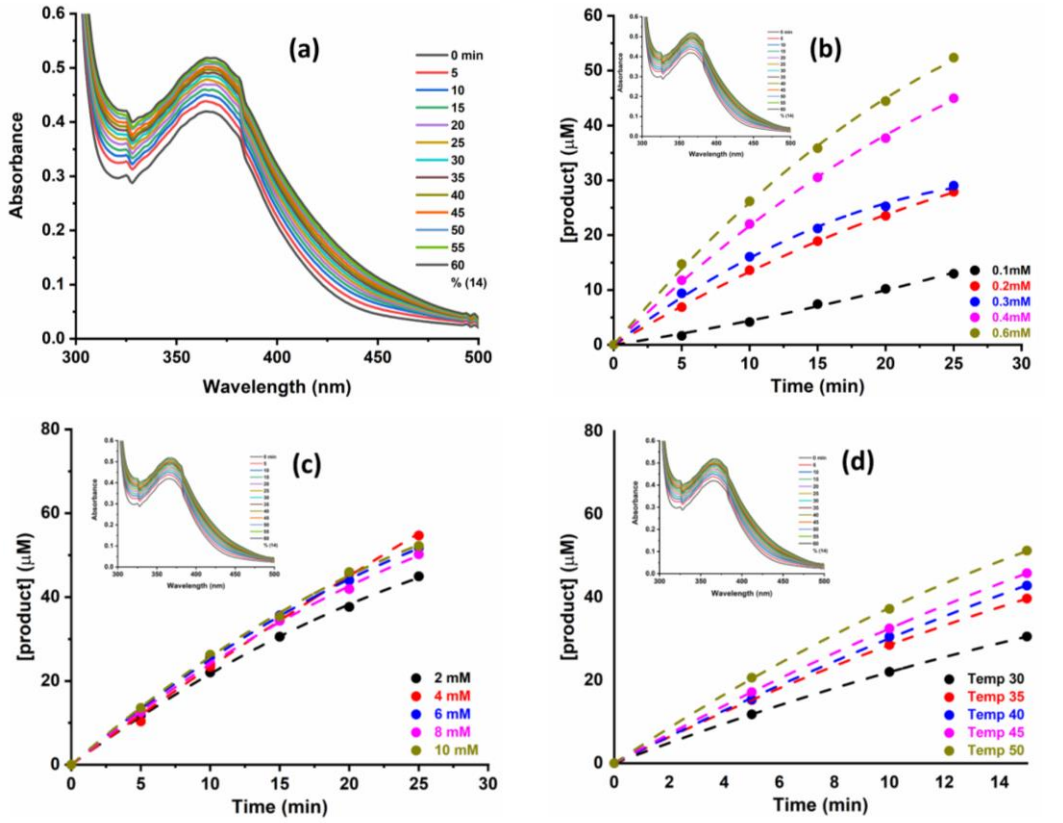

Fig. S5.21 *(a) Time dependent spectral changes over a time period of 0-15min in 4-MC corresponding to* ***C13*** *catalyzed oxidation and (b-d) Plot of [product] as function of time with respect to. substrate (b), catalyst (c) and temperature (d) (Inset: Plot of absorbance vs wavelength at different time interval) for complex* ***C13*** *with 4-MC*

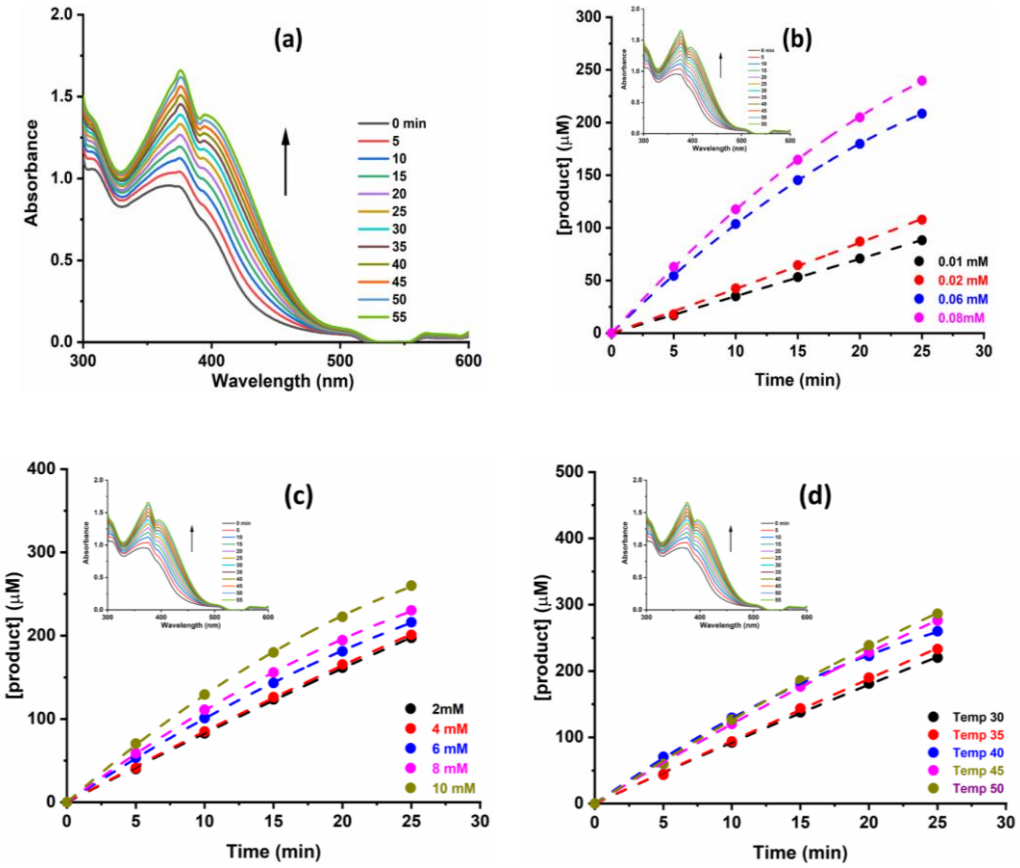

Fig. S5.22 *(a) Time dependent spectral changes over a time period of 0-25min in 3,5-DTBC corresponding to* ***C14*** *catalyzed oxidation and (b-d) Plot of [product] as function of time with respect to substrate (b), catalyst (c) and temperature (d) (Inset: Plot of absorbance vs wavelength at different time interval) for complex* ***C14*** *with 3,5-DTBC*

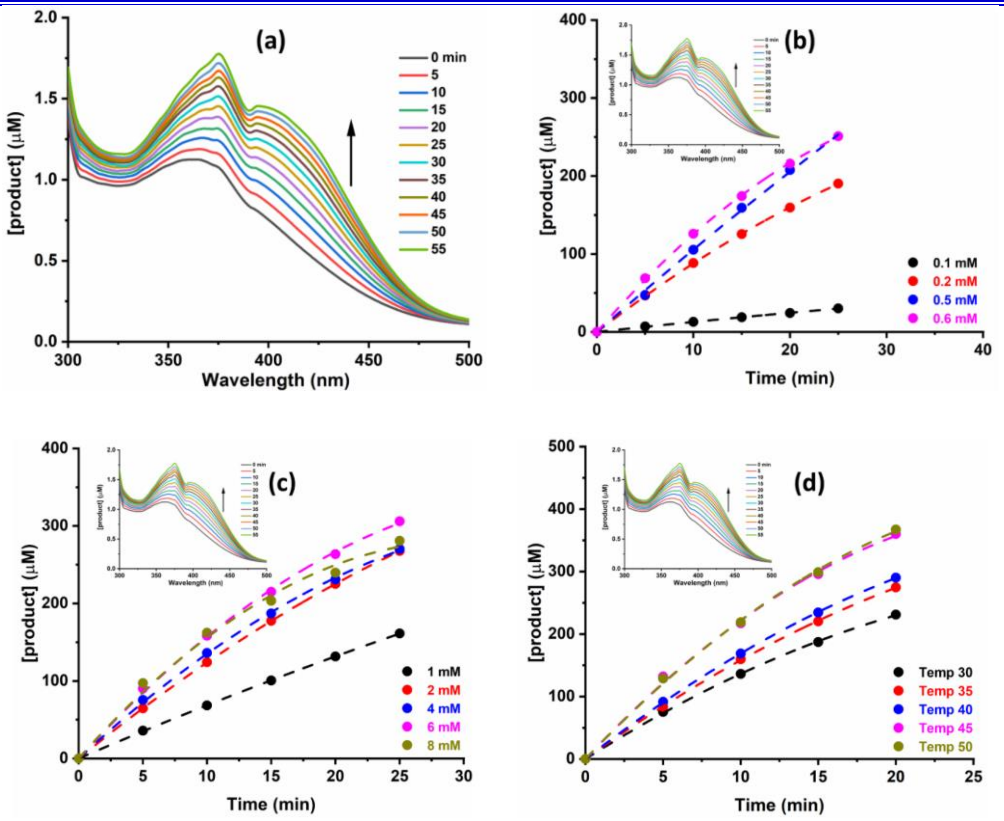

Fig. S5.23 *(a) Time dependent spectral changes over a time period of 0-20 min in 3,5-DTBC corresponding to* ***C15*** *catalyzed oxidation and (b-d) Plot of [product] as function of time with respect to substrate (b), catalyst (c) and temperature (d) (Inset: Plot of absorbance vs wavelength at different time interval) for complex* ***C15*** *with 3,5-DTBC*

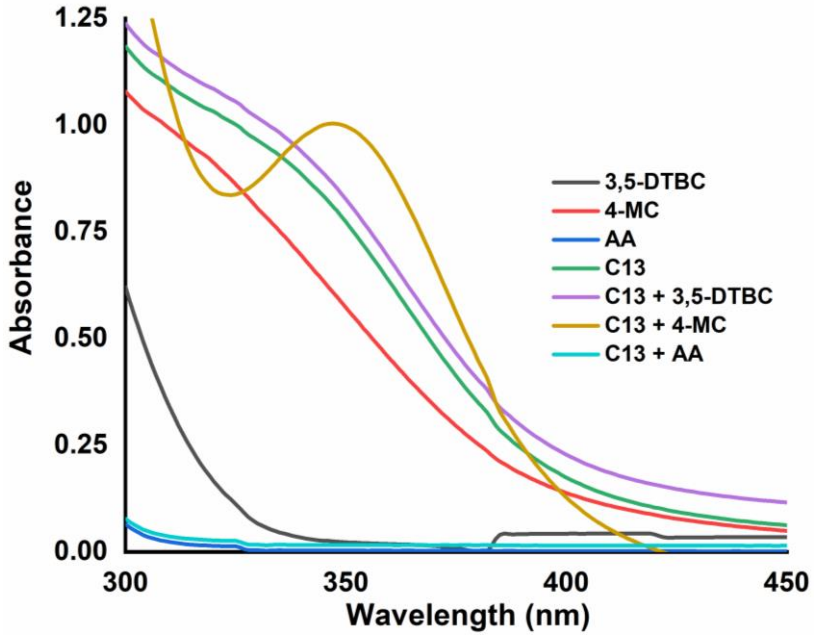

Fig. S5.24 *Electronic spectra of the formation of I_3^- ion in the presence of H_2O_2 (detection was achieved as mentioned in the text)*

Similarly, detection of hydrogen peroxide was spectroscopically monitored for complex **C14** and **C15** for 3,5-BTBC, there was no absorption band due to I_3^- was observed. This confirms that hydrogen peroxide was not formed during the catalytic reaction.

REFERENCES

1. Bailey, N. A., Fenton, D. E., Moody, R., Scrimshire, P. J. & Latour, J.-M. The coexistence of two hydroxo-bridged and one bis-hydroxo dicopper(II) Complexes of 2,6-Bis-((salicylideneamino)methyl)-4-nitrophenol: a comment on the need for flexibility in dinuclear models for haemocyanins. *Inorganica Chim. Acta* **124**, L1–L3 (1986).
2. Adams, H., Bailey, N. A., Fenton, D. E., Moody, R. & Latour, J. M. Observations on the structure and magnetic properties of dinuclear copper(II) complexes derived from flexible dinucleating schiff base ligands. *Inorganica Chim. Acta* **135**, L1–L3 (1987).
3. Bailey, N. A., Fenton, D. E., Moody, R., Scrimshire, P. J., Beloritzky, E., Fries, P. H. & Latour, J.-M. Complexes of ligands providing endogenous bridges. Part 6. The X-ray crystal structure and magnetic properties of a hexanuclear copper(II) aggregate bearing μ3-Cu3(OH) cores supported by 4-nitro-2,6-bis[(salicylideneamino)methyl]phenolate ligands. *J. Chem. Soc. Dalt. Trans.* 2817–2824 (1988).
4. Kumar, D. S., Aruna, V. A. J. & Alexander, V. Synthesis of homodinuclear lanthanide(III) complexes of 24-membered tetraaza and 34-membered octaaza Schiff base macrocycles. *Polyhedron* **18**, 3123–3128 (1999).
5. Kulkarni, A., Avaji, P. G., Bagihalli, G. B., Patil, S. A. & Badami, P. S. Synthesis, spectral, electrochemical and biological studies of Co(II), Ni(II) and Cu(II) complexes with Schiff bases of 8-formyl-7-hydroxy-4-methyl coumarin. *J. Coord. Chem.* **62**, 481–492 (2009).
6. Potapov, A. S., Nudnova, E. A., Domina, G. A., Kirpotina, L. N., Quinn, M. T., Khlebnikov, A. I. & Schepetkin, I. A. Synthesis, characterization and potent superoxide dismutase-like activity of novel bis(pyrazole)-2,2′-bipyridyl mixed ligand copper(ii) complexes. *Dalt. Trans.* 4488–4498 (2009).
7. Patel, M. N., Gandhi, D. S. & Parmar, P. A. SOD mimic activity, DNA binding and in-vitro antibacterial studies of drug based copper(II) complexes. *Inorg. Chem. Commun.* **13**, 618–621 (2010).
8. Patel, M. N., Patel, C. R. & Joshi, H. N. Metal-based biologically active compounds: Synthesis, characterization, DNA interaction, antibacterial, cytotoxic and SOD mimic activities. *Appl. Biochem. Biotechnol.* **169**, 1329–1345 (2013).
9. Patel, M. N., Bhatt, B. S. & Dosi, P. A. Study of SOD mimic and nucleic acid interaction activity exerted by enrofloxacin-based copper(II) complexes. *Chem. Biodivers.* **9**, 2810–2824 (2012).
10. Frisch, M. J., Trucks, G. W., Schlegel, H. B., Scuseria, G. E., Robb, M. A., Cheeseman, J. R., Scalmani, G., Barone, V., Petersson, G. A., Nakatsuji, H., Li, X., Caricato, M., Marenich, A. V., Bloino, J., Janesko, B. G., Gomperts, R., Mennucci, B., Hratchian, H. P., Ortiz, J. V. *et al.* Gaussian 16, Revision A.03. *Gaussian, Inc., Wallingford CT* (2016).
11. Stephens, P. J., Devlin, F. J., Chabalowski, C. F. & Frisch, M. J. Ab Initio Calculation of Vibrational Absorption and Circular Dichroism Spectra Using Density Functional Force Fields. *J. Phys. Chem.* **98**, 11623–11627 (1994).
12. Hay, P. J. & Wadt, W. R. Ab initio effective core potentials for molecular calculations. Potentials for K to Au including the outermost core orbitals. *J. Chem. Phys.* **82**, 299–310 (1985).

13. Wadt, W. R. & Hay, P. J. Ab initio effective core potentials for molecular calculations. Potentials for main group elements Na to Bi. *J. Chem. Phys.* **82**, 284–298 (1985).
14. Dennington, R., Keith, T. A. & Millam, J. M. GaussView, Version 6. at (2016).
15. Lever, A. B. P. (Alfred B. P. *Inorganic electronic spectroscopy, Elsevier, New York*. (Elsevier Pub. Co, 1968).
16. Shoba, D., Periandy, S., Karabacak, M. & Ramalingam, S. Vibrational spectroscopy (FT-IR and FT-Raman) investigation, and hybrid computational (HF and DFT) analysis on the structure of 2,3-naphthalenediol. *Spectrochim. Acta Part A Mol. Biomol. Spectrosc.* **83**, 540–552 (2011).
17. Fukui, K. Role of Frontier Orbitals in Chemical Reactions. *Science (80-.).* **218**, 747–754 (1982).
18. Wang, Q., Chen, D., Liu, X. & Zhang, L. Theoretical mechanisms of the superoxide radical anion catalyzed by the nickel superoxide dismutase. *Comput. Theor. Chem.* **966**, 357–363 (2011).
19. Jawaria, R., Hussain, M., Khalid, M., Khan, M. U., Tahir, M. N., Naseer, M. M., Braga, A. A. C. & Shafiq, Z. Synthesis, crystal structure analysis, spectral characterization and nonlinear optical exploration of potent thiosemicarbazones based compounds: A DFT refine experimental study. *Inorganica Chim. Acta* **486**, 162–171 (2019).
20. Koopmans, T. Über die Zuordnung von Wellenfunktionen und Eigenwerten zu den Einzelnen Elektronen Eines Atoms. *Physica* **1**, 104–113 (1934).
21. Patel, R. N., Singh, N. & Gundla, V. L. N. Synthesis, characterization and superoxide dismutase activity of some octahedral nickel(II) complexes. *Polyhedron* **26**, 757–762 (2007).
22. Patel, R. N. Synthesis, characterization and superoxide dismutase activity of some four coordinated copper(ii) complexes. *Indian J. Chem. - Sect. A Inorganic, Phys. Theor. Anal. Chem.* **48**, 1370–1377 (2009).
23. Patel, R. N., Singh, N., Shukla, K. K. & Gundla, V. L. N. E.S.R., magnetic, electronic and superoxide dismutase studies of imidazolate-bridged Cu(II)-Cu(II) complexes with ethylenediamine as capping ligand. *Spectrochim. Acta - Part A Mol. Biomol. Spectrosc.* **61**, 1893–1897 (2005).
24. He, S.-B., Hu, A.-L., Zhuang, Q.-Q., Peng, H.-P., Deng, H.-H., Chen, W. & Hong, G.-L. Ascorbate Oxidase Mimetic Activity of Copper(II) Oxide Nanoparticles. *ChemBioChem* **21**, 978–984 (2020).
25. Monzani, E., Battaini, G., Perotti, A., Casella, L., Gullotti, M., Santagostini, L., Nardin, G., Randaccio, L., Geremia, S., Zanello, P. & Opromolla, G. Mechanistic, structural, and spectroscopic studies on the catecholase activity of a dinuclear copper complex by dioxygen. *Inorg. Chem.* **38**, 5359–5369 (1999).
26. Monzani, E., Quinti, L., Perotti, A., Casella, L., Gullotti, M., Randaccio, L., Geremia, S., Nardin, G., Faleschini, P. & Tabbì, G. Tyrosinase models. Synthesis, structure, catechol oxidase activity, and phenol monooxygenase activity of a dinuclear copper complex derived from a triamino pentabenzimidazole ligand. *Inorg. Chem.* **37**, 553–562 (1998).
27. Ackermann, J., Meyer, F., Kaifer, E. & Pritzkow, H. Tuning the Activity of Catechol Oxidase Model Complexes by Geometric Changes of the Dicopper Core. *Chem. – A Eur. J.* **8**, 247–258 (2002).
28. Liu, C., Cai, Y., Wang, J., Liu, X., Ren, H., Yan, L., Zhang, Y., Yang, S., Guo, J. &

Liu, A. Facile Preparation of Homogeneous Copper Nanoclusters Exhibiting Excellent Tetraenzyme Mimetic Activities for Colorimetric Glutathione Sensing and Fluorimetric Ascorbic Acid Sensing. *ACS Appl. Mater. Interfaces* **12**, 42521–42530 (2020).

29. Guo, D., Li, C., Liu, G., Luo, X. & Wu, F. Oxidase Mimetic Activity of a Metalloporphyrin-Containing Porous Organic Polymer and Its Applications for Colorimetric Detection of Both Ascorbic Acid and Glutathione. *ACS Sustain. Chem. Eng.* **9**, 5412–5421 (2021).
30. González-Álvarez, M., Alzuet, G., Borrás, J., García-Granda, S. & Montejo-Bernardo, J. M. Structural and functional models for the dinuclear copper active site in catechol oxidases: Synthesis, X-ray crystal structures, magnetic and spectroscopic properties of μ-methoxo-bridged dinuclear copper(II) complexes with N-substituted sulfonamide ligan. *J. Inorg. Biochem.* **96**, 443–451 (2003).
31. Anbu, S. & Kandaswamy, M. Electrochemical, magnetic, catalytic, DNA binding and cleavage studies of new mono and binuclear copper(II) complexes. *Polyhedron* **30**, 123–131 (2011).
32. Selmeczi, K., Réglier, M., Giorgi, M. & Speier, G. Catechol oxidase activity of dicopper complexes with N-donor ligands. *Coord. Chem. Rev.* **245**, 191–201 (2003).
33. Zippel, F., Ahlers, F., Werner, R., Haase, W., Nolting, H. F. & Krebs, B. Structural and functional models for the dinuclear copper active site in catechol oxidases: Syntheses, X-ray crystal structures, magnetic and spectral properties, and x-ray absorption spectroscopic studies in solid state and in solution. *Inorg. Chem.* **35**, 3409–3419 (1996).
34. Dutta, S., Mayans, J. & Ghosh, A. Facile synthesis of a new Cu(II) complex with an unsymmetrical ligand and its use as an O3 donor metalloligand in the synthesis of Cu(II)-Mn(II) complexes: Structures, magnetic properties, and catalytic oxidase activities. *Dalt. Trans.* **49**, 1276–1291 (2020).

•